

The *Herschel* view of the nebula around the luminous blue variable star AG Carinae^{★,★★,★★★}

C. Vamvatira-Nakou¹, D. Hutsemékers^{1,★★★★}, P. Royer², N. L. J. Cox², Y. Nazé^{1,†}, G. Rauw¹,
C. Waelkens², and M. A. T. Groenewegen³

¹ Institut d'Astrophysique et de Géophysique, Université de Liège, Allée du 6 août, 17 – Bât. B5c, 4000 Liège, Belgium
e-mail: vamvatira@astro.ulg.ac.be

² Instituut voor Sterrenkunde, KU Leuven, Celestijnenlaan 200D, Bus 2401, 3001 Leuven, Belgium

³ Koninklijke Sterrenwacht van België, Ringlaan 3, 1180 Brussels, Belgium

Received 1 October 2014 / Accepted 24 March 2015

ABSTRACT

Far-infrared *Herschel* PACS imaging and spectroscopic observations of the nebula around the luminous blue variable (LBV) star AG Car have been obtained along with optical imaging in the H α +[N II] filter. In the infrared light, the nebula appears as a clumpy ring shell that extends up to 1.2 pc with an inner radius of 0.4 pc. It coincides with the H α nebula, but extends further out. Dust modeling of the nebula was performed and indicates the presence of large grains. The dust mass is estimated to be $\sim 0.2 M_{\odot}$. The infrared spectrum of the nebula consists of forbidden emission lines over a dust continuum. Apart from ionized gas, these lines also indicate the existence of neutral gas in a photodissociation region that surrounds the ionized region. The abundance ratios point towards enrichment by processed material. The total mass of the nebula ejected from the central star amounts to $\sim 15 M_{\odot}$, assuming a dust-to-gas ratio typical of LBVs. The abundances and the mass-loss rate were used to constrain the evolutionary path of the central star and the epoch at which the nebula was ejected, with the help of available evolutionary models. This suggests an ejection during a cool LBV phase for a star of $\sim 55 M_{\odot}$ with little rotation.

Key words. circumstellar matter – stars: massive – stars: mass-loss – stars: variables: S Doradus – stars: individual: AG Carinae

1. Introduction

The term “luminous blue variable” (LBV) was used by Conti (1984) for the first time and referred to hot luminous massive variable stars that are evolved, but are not Wolf-Rayet (WR) stars. Nowadays, LBVs, also known as S Doradus variables, are considered to be massive evolved stars mainly characterized by a) high luminosity, $\sim 10^6 L_{\odot}$; b) photometric variability with amplitudes from ~ 0.1 mag (small oscillations) up to ≥ 2 mag (giant eruptions); and c) high mass-loss rates $\sim 10^{-5} - 10^{-4} M_{\odot} \text{ yr}^{-1}$ (Humphreys & Davidson 1994). Their location on the Hertzsprung–Russell (HR) diagram is in the upper left part although some of them undergo occasional excursions to the right.

An early-type O star with initial mass $\geq 30 M_{\odot}$ evolves to a WR star by losing a significant fraction of its initial mass. Luminous blue variables represent a short stage ($\sim 10^4 - 10^5$ yr) in this evolutionary path according to current evolutionary scenarios (Maeder & Meynet 2010). Although stellar winds can be responsible for stellar mass-loss, the mass-loss rates of O stars have been revised downward in the past few years (Bouret et al. 2005; Fullerton et al. 2006; Puls et al. 2008). Consequently, episodes of extreme mass-loss during an

intermediate evolutionary phase, like a LBV or a red supergiant (RSG) phase, are now thought to play a key role, which is why the study of the LBVs and their circumstellar environments is crucial for understanding massive star evolution.

Such extreme mass-loss leads to the formation of ejected nebulae, which have been observed around many LBVs (Hutsemékers 1994; Nota et al. 1995). They are classified into three categories according to their morphology: shell nebulae, filamentary nebulae and peculiar morphologies (Nota et al. 1995). The study of these circumstellar environments can reveal the mass-loss history of the central star since they are formed by the material that has been ejected from the central star in a previous evolutionary phase. Dust and molecular gas (CO) have been revealed by infrared and millimeter studies of LBV nebulae (McGregor et al. 1988; Hutsemékers 1997; Nota et al. 2002).

Some LBVs are surrounded by more than one nebulae. This is the case of the LBV G79.29+0.46. Near-infrared and millimeter data analyzed by Jiménez-Esteban et al. (2010) revealed multiple shells around this star. Infrared observations by the *Herschel* Space Observatory (Pilbratt et al. 2010) revealed a second nebula around the LBV WRAY 15-751 (Vamvatira-Nakou et al. 2013)

AG Car (=HD 94910 =IRAS 10541-6011) is a well-studied prototypical LBV. Its variability was first discovered by Wood (1914). It was first classified as a P Cygni star by Cannon (1916) and finally classified as a LBV by Humphreys (1989). Numerous studies show that this star exhibits photometric and spectroscopic variability. In the optical *V*-band, the photometric changes during the S Dor cycle are about 2 mag on a timescale of 5–10 years (Stahl 1986; van Genderen et al. 1988; Leitherer et al. 1992; Sterken et al. 1996). In addition, smaller variations

* *Herschel* is an ESA space observatory with science instruments provided by European-led Principal Investigator consortia and with important participation from NASA.

** Based in part on observations collected at the European Southern Observatory, La Silla, Chile.

*** Appendices are available in electronic form at

<http://www.aanda.org>

**** Senior Research Associate FNRS.

† Research Associate FNRS.

of 0.1–0.5 mag on a timescale of about 1 year were discovered (van Genderen et al. 1997). During the periods of visual minimum, AG Car has a spectrum of a WR star, with Ofpe/WN9 spectral type according to Stahl (1986) and with WN11 according to a more recent study by Smith et al. (1994). During the periods of visual maximum, AG Car’s spectrum corresponds to that of an early-A hypergiant (Wolf & Stahl 1982; Stahl et al. 2001).

Humphreys et al. (1989) concluded that the distance to AG Car is 6 ± 1 kpc, based on the calculated kinematic distance and on the observed variation of the interstellar extinction with distance. This result was confirmed by Hoekzema et al. (1992), based again on the extinction versus distance relation. Stahl et al. (2001) suggested a slightly lower distance of 5–6 kpc based on their calculations of the heliocentric systemic velocity of AG Car (10 ± 5 km s⁻¹), which is compatible with the value of Humphreys et al. (1989) considering the errors. Groh et al. (2009) calculated a similar systemic velocity. Consequently, the value of 6 ± 1 kpc that encompasses all measurements is adopted for all calculations in this study.

Lamers et al. (1989) calculated $\log L/L_{\odot} = 6.2 \pm 0.2$ for the luminosity of AG Car and showed that it remains constant during the light variations of the star, as was also found for other LBVs (R71: Wolf et al. 1981; R127: Stahl & Wolf 1986). Later on, Leitherer et al. (1994), in their study of the stellar wind of AG Car, found a slightly lower bolometric luminosity of 6.0 ± 0.2 based on ultraviolet observations combined with visual and near-infrared photometry. They also confirmed the non-variability of the bolometric luminosity during the S Dor cycle. Given such a high value of bolometric luminosity, AG Car is well above the Humphreys-Davidson limit (Humphreys & Davidson 1979), the limit above which a massive star becomes unstable and high mass loss episodes take place. However, in a recent study of the fundamental parameters of AG Car during visual minima, Groh et al. (2009) concluded that the bolometric luminosity of AG Car does change during the S Dor cycle. They obtained a maximum value of the bolometric luminosity during minimum phase of $\log L/L_{\odot} = 6.18$, with a variation amplitude of $\Delta(\log L/L_{\odot}) \sim 0.17$ dex. This luminosity variation lies inside the limits of the previously calculated values considering the errors. In all these studies, the distance 6 ± 1 kpc was used.

Thackeray (1950) discovered that AG Car is surrounded by a nebulous shell that has the shape of an elliptical ring with nonuniform intensity. He measured the size of the nebula to be $39'' \times 30''$ and the width of the ring to be about $5''$. Stahl (1987) studied direct CCD imaging data of AG Car and suggested that very likely the nebula around this star is the result of a heavy mass-loss episode that took place during an S Dor outburst and not the result of interstellar material that was swept up by the stellar wind. Smith (1991) studied the dynamics of AG Car nebula based on spectroscopic observations in the optical waveband. She measured an average nebular expansion velocity of 70 km s⁻¹ and concluded that the shell expansion is roughly symmetrical. She also reported the presence of a jet-like bipolar mass outflow, expanding with a velocity of 83 km s⁻¹ and distorting the northeastern edge of the shell. Nota et al. (1992) studied the nebula around AG Car using high-resolution coronagraphic imaging and spectroscopic data so as to constrain its geometry. They confirmed the value of the expansion velocity of Smith (1991) and concluded that this nebular shell shows a deviation from spherical symmetry, based on the observed radial velocity variations and on the gas distribution observed in the images.

Voors et al. (2000) studied AG Car in the infrared waveband by modeling ground-based infrared images taken at about $10 \mu\text{m}$ and ISO spectroscopic observations, from which they derived the properties of the circumstellar dust. The dust shell is detached and slightly elongated. The ionized gas appears co-spatial with the dust. Polycyclic aromatic hydrocarbons (PAHs) are present. The dust shell contains mostly large grains, although very large grains are present and also a population of small, warm, out of thermal equilibrium grains that produce continuum and PAH bands emission.

Duncan & White (2002) observed the AG Car nebula at the radio wavelengths (3 and 6 cm). Their 3 cm wavelength radio image revealed a nebula with a detached ring shape, very similar to the morphology in the H α + [NII] filter (see Sect. 3).

Nota et al. (2002) detected ¹²CO $J = 1 \rightarrow 0$ and $J = 2 \rightarrow 1$ emission from AG Car for the first time. The CO line profiles indicate a region of molecular gas that is close to the star, expanding slowly and not originating from the gaseous nebula. They argued that the most plausible scenario to explain the observed profile is the presence of a circumstellar disk.

Weis (2008), using deep H α imaging, reported the presence of diffuse emission in the form of a cone-like extension to the north of the AG Car nebula and concluded that it is clearly part of the nebula. It extends up to $28''$ outside the nebula, increasing its size by about two times. It has a higher radial velocity than the ring.

In this study we present an analysis and discussion of the images and the spectrum of the AG Car nebula taken by PACS (Photodetector Array Camera and Spectrometer, Poglitsch et al. 2010), which is one of the three instruments on board the *Herschel* Space Observatory. The paper is organized as follows. In Sect. 2 the observations and the data reduction procedure are presented. A description of the nebular morphology based on these observations is given in Sect. 3. The dust continuum emission is modeled in Sect. 4, while the emission line spectrum is analyzed in Sect. 5. In Sect. 6 a general discussion is presented and in Sect. 7 conclusions are drawn.

2. Observations and data reduction

2.1. Infrared observations

The infrared observations include imaging and spectroscopy of the AG Car nebula and were carried out using PACS in the framework of the Mass-loss of Evolved StarS (MESS) guaranteed time key program (Groenewegen et al. 2011).

The PACS imaging observations were carried out on August 12, 2010, which corresponds to *Herschel*’s observational day (OD) 456. The observing mode was the scan map in which the telescope slews at constant speed (in our case the “medium” speed of $20''/s$) along parallel lines in order to cover the required area of the sky. Two orthogonal scan maps were obtained for each filter. Our final data set consists of maps at 70, 100 and $160 \mu\text{m}$. The observation identification numbers (obsID) of the four scans are 1342202927, 1342202928, 1342202929, and 1342202930; each scan has a duration of 157s.

To perform the data reduction we used the *Herschel* Interactive Processing Environment (HIPE, Ott 2010) up to level 1. Subsequently, the data were reduced and combined using the Scanamorphos software (Roussel 2013). The pixel size in the final maps is $2''$ in the blue channel (70, $100 \mu\text{m}$) and $3''$ in the red channel ($160 \mu\text{m}$). It should be mentioned that the *Herschel* PACS point spread function (PSF) full widths at half maximum

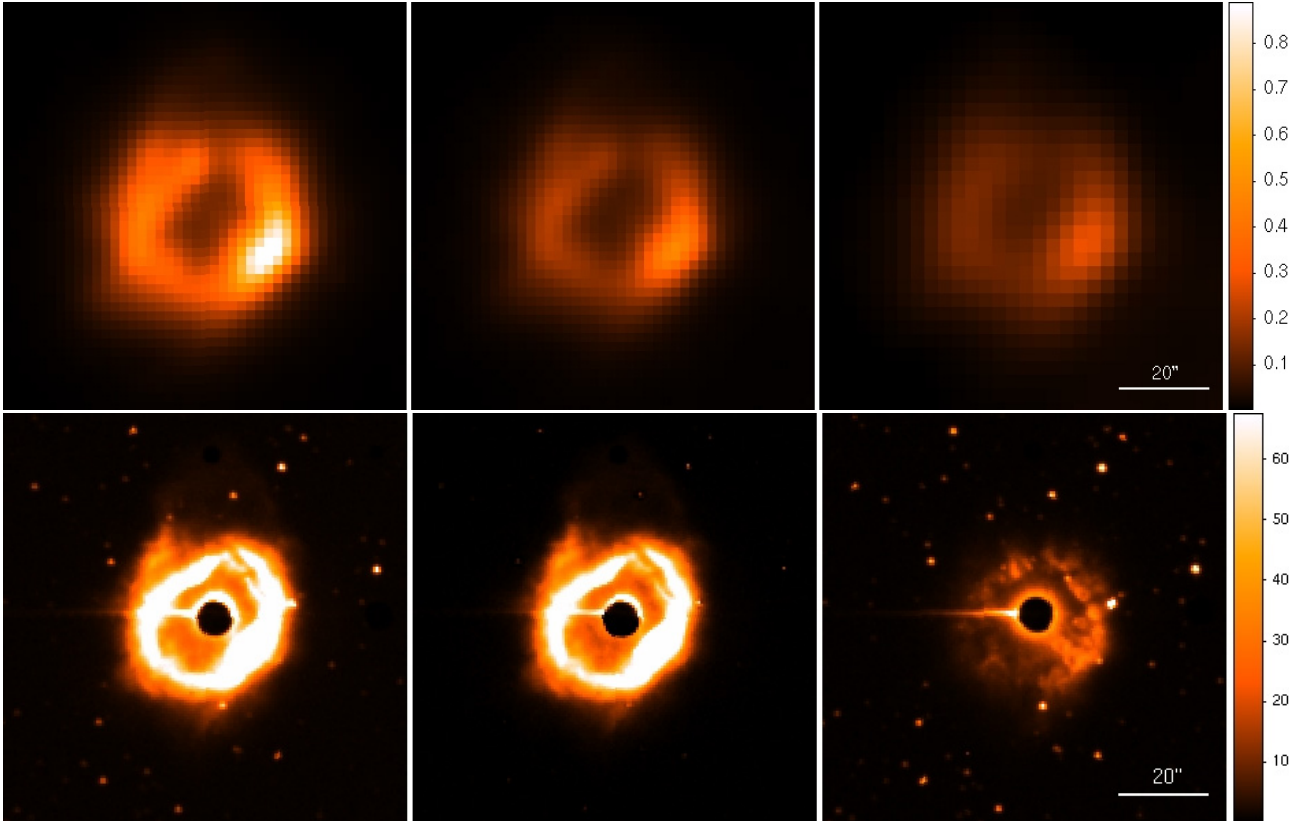


Fig. 1. Images of the nebula around AG Car. *Top:* PACS images at $70\ \mu\text{m}$, $100\ \mu\text{m}$, and $160\ \mu\text{m}$ from *left to right*. *Bottom:* the $\text{H}\alpha + [\text{N II}]$ image (*left*), the continuum image (*right*) and the image resulting from the subtraction of the continuum image from the $\text{H}\alpha + [\text{N II}]$ image after correcting for the position offsets and for the different filter transmissions using field stars (*middle*). The size of each image is $1.5' \times 1.5'$. The scale on the right corresponds to the surface brightness (arbitrary units). North is up and east is to the left.

(FWHMs) are $5''.2$, $7''.7$, and $12''$ at $70\ \mu\text{m}$, $100\ \mu\text{m}$ and $160\ \mu\text{m}$, respectively.

The spectrum of the AG Car nebula was taken on June 5, 2010 (OD 387), with the PACS integral-field spectrometer that covers the wavelength range from $52\ \mu\text{m}$ to $220\ \mu\text{m}$ in two channels that operate simultaneously in the blue $52\text{--}98\ \mu\text{m}$ band (second order: B2A $52\text{--}73\ \mu\text{m}$ and B2B $70\text{--}105\ \mu\text{m}$), and the red $102\text{--}220\ \mu\text{m}$ band (first order: R1A $133\text{--}220\ \mu\text{m}$ and R1B $102\text{--}203\ \mu\text{m}$). Simultaneous imaging of a $47'' \times 47''$ field of view is provided that is resolved in 5×5 square spatial pixels (i.e., spaxels). The two-dimensional field of view is then rearranged along a 1×25 pixel entrance slit for the grating via an image slicer employing reflective optics. Its resolving power is $\lambda/\delta\lambda \sim 940\text{--}5500$ depending on the wavelength. The observing template was the spectral energy distribution (SED) that provides a complete coverage between 52 and $220\ \mu\text{m}$. The two obsIDs are 1342197792 and 1342197793. HIPE was also used for the data reduction. The standard reduction steps were followed and in particular the subtraction of the background spectrum obtained through chopping and nodding.

2.2. Visible observations

The optical images of the AG Car nebulae were obtained on April 6, 1995, with the 3.6 m telescope at the European Southern Observatory (ESO), La Silla, Chile. A series of short (1 s–10 s) and longer (30 s–60 s) exposures were secured in a $\text{H}\alpha + [\text{N II}]$ filter ($\lambda_c = 6560.5\ \text{\AA}$; $\text{FWHM} = 62.2\ \text{\AA}$) and in a continuum filter just redwards ($\lambda_c = 6644.7\ \text{\AA}$; $\text{FWHM} = 61.0\ \text{\AA}$). The EFOSC1

camera was used in its coronagraphic mode: for the longer exposures, the $8''$ circular coronagraphic mask was inserted in the aperture wheel and positioned on the central star while the Lyot stop was inserted in the grism wheel (Melnick et al. 1989). The frames were bias-corrected and flat-fielded. The CCD pixel size was $0''.605$ on the sky. The night was photometric and the seeing around $1''.2$. In order to properly calibrate the images, three spectrophotometric standard stars and three planetary nebulae with known $\text{H}\alpha$ flux were observed in the $\text{H}\alpha + [\text{N II}]$ filter.

3. Morphology of the nebula

The three PACS infrared images of the nebula around the LBV AG Car at $70\ \mu\text{m}$, $100\ \mu\text{m}$, and $160\ \mu\text{m}$ along with images taken at optical wavelengths are shown in Figs. 1 and 2.

The infrared images reveal a dusty shell nebula with a clumpy ring morphology that is clearly detached from the central star (not visible at these wavelengths). The brightness of the nebula is not uniform, with the southwestern part being the brightest one. This agrees with the nonuniform brightness of the images at $12.5\ \mu\text{m}$ and $12.78\ \mu\text{m}$ analyzed by Voors et al. (2000). An axis at position angle (PA) $\sim 160^\circ$ can be defined (north: PA = 0° ; east: PA = 90°). Cuts of the $70\ \mu\text{m}$ PACS image through PA $\sim 160^\circ$ and PA $\sim 70^\circ$ (Fig. 4) show peaks at a radius of about $14''$, although with different intensities. The ring extends up to $\sim 42''$. These values correspond to $0.4\ \text{pc}$ and $1.2\ \text{pc}$, respectively, at a distance of 6 kpc. On top of this central circular nebula, there is a northern faint extension. No other more extended nebula associated with the star can be detected. A three-color infrared image of the nebula and its environment is illustrated in Fig. 3, which

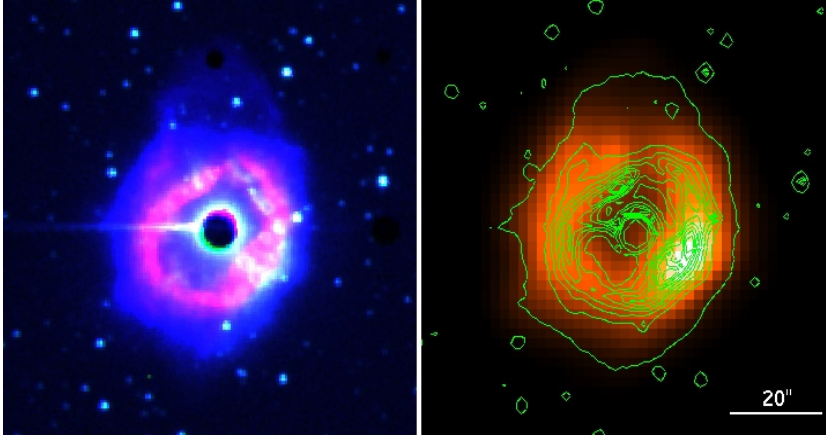


Fig. 2. *Left:* view of the nebula in the optical. The bright $H\alpha + [N II]$ ring nebula is illustrated in red (also shown in Fig. 1 at the same scale) while the fainter $H\alpha + [N II]$ emission is shown in blue, differently scaled in surface brightness, revealing the northern extension (Weis 2008). The continuum image that outlines the dust scattered nebula is presented in green. *Right:* contour image of the optical emission from the nebula (green lines) superposed on the infrared image of the nebula at $70 \mu m$ (also shown in Fig. 1 at the same scale). The size of each image is $1.5' \times 1.5'$. North is up and east is to the left.

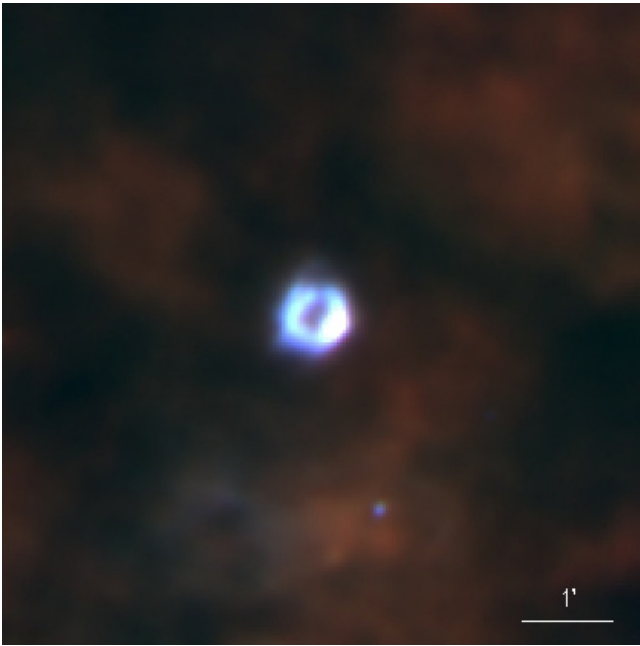


Fig. 3. Three-color image ($70 \mu m$ in blue, $100 \mu m$ in green and $160 \mu m$ in red) of the AG Car nebula. The LBV nebula appears located inside a cavity in the interstellar medium. The size of the image is $7' \times 7'$. North is up and east is to the left.

shows best this faint northern extension first reported by Weis (2008), although the resolution is not good enough to reveal its detailed structure. The LBV nebula seems to be located in a cavity in the interstellar medium, probably excavated by the star in a previous evolutionary phase. The radius of this empty cavity is about $2.5'$, which corresponds to 4.4 pc at a distance of 6 kpc .

The $H\alpha + [N II]$ image (Fig. 1) shows that the gas nebula around AG Car forms an elliptical shell with an average outer radius of $\sim 20''$ and an inner radius of $\sim 11''$. To more accurately investigate the morphology of the nebula in the optical, a three-color image is presented in Fig. 2. The fainter nebular optical emission reveals the northern extension described in Weis (2008). The nebula that surrounds the bright ring extends up to $\sim 23''$, while the north extension goes up to $\sim 36''$ from the center of the nebula. These numbers correspond to 0.7 pc and 1 pc , respectively, at a distance of 6 kpc , in agreement with the size of the nebula given in Weis (2008, 2011).

In the $H\alpha$ light, the dynamics points to a spherically expanding shell distorted by a more extended bipolar nebula (Smith 1991; Nota et al. 1992). In projection on the sky, the shell

appears as an elliptical ring with $PA \sim 131^\circ$, different from the infrared shell PA . Nevertheless, the contour image of the optical emission (both bright and faint) superimposed on the infrared image of the nebula at $70 \mu m$ as illustrated in the right panel of Fig. 2 shows that the overall morphology of the gas nebula is similar to the infrared dust morphology, although the $H\alpha + [N II]$ ring nebula appears slightly smaller and more elliptical than the infrared nebula. The bright region at the southwestern part of the gas nebula coincides with the bright region of the infrared dust nebula. The northern faint extended structure, which appears both in the infrared and in the optical, is likely a lobe of the bipolar nebula. The extension seen to the south in the $H\alpha + [N II]$ map and in the velocity maps of Smith (1991) could constitute a part of a second fainter lobe. The system may thus consist of a typical bipolar nebula seen roughly through the poles (i.e., at inclination $\lesssim 30^\circ$), with two faint lobes and a bright waist.

The nebula is also clearly detected in the optical continuum filter (Fig. 1), indicating significant dust scattering. The morphology of the dust reflection nebula appears somewhat different from the morphology of the $H\alpha + [N II]$ emission. This reflection nebula around AG Car was first described in Paresce and Nota (1989) and its stunning structure resolved with the Hubble Space Telescope (Nota et al. 1995, 1996). More specifically, in the optical continuum image (Figs. 1 and 2) the ring appears circular and very clumpy with a jet-like feature that starts from the central part of the nebula and extends towards the southwestern part, which is the brightest region of the dust and gas emission. The northern extension of the nebula is not detected in the optical continuum. As does the $H\alpha + [N II]$ ring nebula, the optical continuum emission appears slightly inside the infrared continuum emission, although a detailed comparison is difficult given the lower spatial resolution of the PACS images. The difference in morphology between the optical continuum and the $H\alpha + [N II]$ nebulae may arise from anisotropic illumination and thus ionization of different parts of the nebula owing to its clumpy structure.

Considering the nebular expansion velocity, v_{exp} , of 70 km s^{-1} measured by Smith (1991), the kinematic age, t_{kin} , of the nebula can be estimated. As mentioned above, the nebula in the infrared extends to 1.2 pc in radius, r , so it has a kinematic age of $t_{\text{kin}} = r/v_{\text{exp}} = 1.7 \times 10^4$ years. The temporal difference between the inner and the outer radius of the nebula is 1.1×10^4 years.

4. Dust continuum emission

Integrated flux densities were derived for the nebular shell at the three PACS wavelengths by performing aperture photometry on

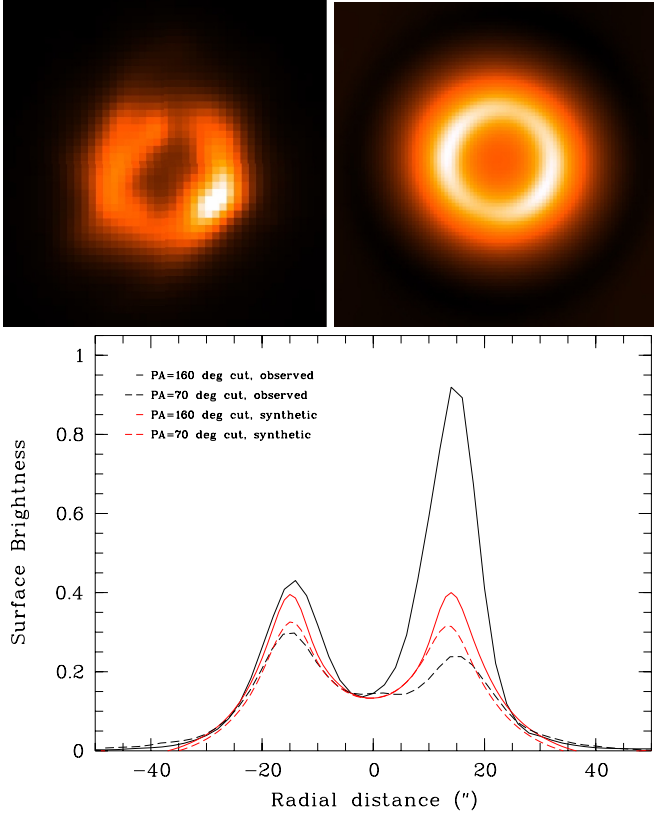


Fig. 4. *Top left:* the $1.5' \times 1.5'$ image of the nebula around AG Car observed with PACS at $70 \mu\text{m}$. North is up and east to the left. *Top right:* the synthetic image computed with 2-Dust using $r_{\text{in}} = 14''$ and $r_{\text{out}} = 42''$ and convolved with the PACS PSF. *Bottom:* cuts with PA = 160° and 70° through the central part of the nebula at $70 \mu\text{m}$, observed (black) and synthetic (red) ones.

the PACS images. We also used imaging data taken from the archives of the Infrared Astronomical Satellite (IRAS) mission (Neugebauer et al. 1984) and the Infrared Astronomical Mission AKARI (Murakami et al. 2007). In these archival data we did not include the IRAS observation at $12 \mu\text{m}$ because it is only an upper limit or at $100 \mu\text{m}$ because it is not of high quality. We note that the beam size of the IRAS and AKARI observations is large enough to fully encompass the ring nebula around AG Car. Images from the SPIRE (Spectral and Photometric Imaging Receiver, Griffin et al. 2010) instrument on board the *Herschel* Space Observatory were also included. They were taken from the observations of the *Herschel* Infrared Galactic Plane survey (Hi-GAL, Molinari et al. 2010) made immediately public for legacy. The Hi-GAL observations of the field around AG Car were retrieved from the archive processed up to level 2. Only the maps at $250 \mu\text{m}$ and at $350 \mu\text{m}$ were used, because at $500 \mu\text{m}$ the nebula is very faint so that flux determination is highly uncertain. Integrated flux densities were derived for the nebular shell at these two SPIRE wavelengths by performing aperture photometry on the images.

We applied photometric color correction to all flux densities derived from the observations of these three space missions. With this correction, the monochromatic flux densities that refer to a constant energy spectrum are converted to the true object SED flux densities at the photometric reference wavelengths of each instrument. We used the flux density ratio to derive the color temperature for the color correction of the IRAS data and then we chose the corresponding color-correction factor

Table 1. Color-corrected nebular flux densities.

Spacecraft-Instrument	Date	λ (μm)	F_ν (Jy)	Error (Jy)
IRAS ^a	1983	25	187.5	9.4
		60	177.7	28.4
AKARI-IRC ^b	2007	9	9.04	0.14
		18	119.2	0.24
AKARI-FIS ^c	2007	65	229.3	6.53
		90	81.0	3.9
		140	45.5	5.2
		160	35.1	4.6
<i>Herschel</i> -PACS ^d	2010	70	173	2
		100	103	3
		160	42	3
<i>Herschel</i> -SPIRE ^e	2010	250	8.1	2
		350	3.0	1

Notes. Data from: ^(a) IRAS Point Source Catalog (Beichman et al. 1988), ^(b) Akari/IRC Point Source Catalogue (Ishihara et al. 2010), ^(c) Akari/FIS Bright Source Catalogue (Yamamura et al. 2010), ^(d) This work, ^(e) Observations of Hi-GAL (Molinari et al. 2010) retrieved from the *Herschel* archive.

(Beichman et al. 1988). The ratio $R(25,60)$ corresponds to a temperature of 140 K, so the correction factors for this temperature were used. To color correct the AKARI FIS and IRC data we fitted a blackbody to the two data sets independently using the $25 \mu\text{m}$ IRAS observation because we needed a measurement near the maximum of the curve. These fits led us to adopt the color-correction factors that correspond to a temperature of 150 K for FIS (Yamamura et al. 2010) and 220 K for IRC data (Lorente et al. 2008). To estimate the color correction of the *Herschel*-PACS data, we fitted a blackbody, considering again the $25 \mu\text{m}$ IRAS observation. This fit gave a temperature of 150 K, for which we adopted the corresponding correction factor (Müller et al. 2011). For the SPIRE data, the instructions for color correction given in the SPIRE Handbook¹, were followed.

The corrected measurements are presented in Table 1. They enabled us to construct the infrared SED of the nebula, along with the archived spectrum that was part of the observations carried out by the Infrared Space Observatory (ISO) mission (Kessler et al. 1996). A detailed discussion on this ISO-LWS spectrum can be found in Voors et al. (2000).

The infrared SED of the nebula around AG Car obtained at different epochs with the various instruments is shown in Fig. 5. All these measurements agree very well within the uncertainties except the one at $90 \mu\text{m}$. This is likely due to the uncertainty on the color correction that was stronger for the $90 \mu\text{m}$ (AKARI-FIS) data point.

A model of the dust nebula around the LBV AG Car has been carried out in the past by Voors et al. (2000). They used a one-dimensional radiative transfer code to fit both imaging and spectroscopic infrared data. To further constrain the dust properties, we use the AKARI archive imaging data and the new PACS and SPIRE imaging data in addition to the IRAS imaging data and the ISO infrared spectrum. The PACS imaging allows us to measure the nebular radius at the wavelengths of the bulk of dust emission. To model the dust shell we only considered the spectrum at $\lambda > 20 \mu\text{m}$. The spectrum at $\lambda < 12 \mu\text{m}$ comes from the central star that Voors et al. (2000) fitted with a spherical non-LTE model atmosphere. For the spectrum between $\lambda \sim 14$ and

¹ http://herschel.esac.esa.int/Docs/SPIRE/spire_handbook.pdf

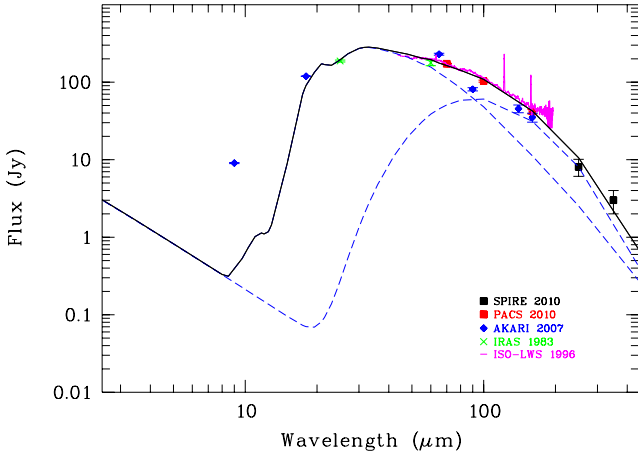


Fig. 5. Infrared SED of the nebula around the LBV AG Car from data collected at different epochs: the ISO-LWS spectrum and color-corrected photometric measurements from IRAS, AKARI and *Herschel* (PACS and SPIRE) space observatories. Results of the 2-Dust model fitting are illustrated. Data at $\lambda < 20 \mu\text{m}$ are not considered in the fit. The best fit (solid line) is achieved considering two populations of dust grains (dashed lines).

$20 \mu\text{m}$ they argued that it too likely comes from the central star and not from some extended source.

The two-dimensional radiative transfer code 2-Dust (Ueta & Meixner 2003) was used to model and interpret the dust emission spectrum and the far-infrared images. This is a publicly available versatile code that can be supplied with various grain size distributions and optical properties as well as complex axisymmetric density distributions.

It should be mentioned here that since the PACS spectral field of view is smaller than the nebular size, the PACS spectrum was not taken into consideration for the dust model as this spectrum is indeed fainter than the PACS photometric points that contain the total flux of the nebula.

To model the PACS ring of dust with the code 2-Dust, it is necessary to consider the morphology of the nebula revealed through the infrared PACS and the optical images so as to choose the best geometric parameters for the axisymmetric dust density distribution model. The 2-Dust code uses a normalized density distribution function (Meixner et al. 2002) that is based on a layered shell model,

$$\rho(R, \theta) = \left(\frac{R}{R_{\min}} \right)^{-B} \left\{ 1 + C \sin^F \theta \left[e^{-(R/R_{\text{sw}})^D} / e^{-(R_{\min}/R_{\text{sw}})^D} \right] \right\} \times \left\{ 1 + A(1 - \cos \theta)^F \left[e^{-(R/R_{\text{sw}})^E} / e^{-(R_{\min}/R_{\text{sw}})^E} \right] \right\}, \quad (1)$$

where $\rho(R, \theta)$ is the dust mass density at radius R and latitude θ , R_{\min} is the inner radius of the shell, and R_{sw} is the superwind radius that defines the boundary between the spherical wind and the axisymmetric superwind. The first term represents the radial profile of the spherical wind; the parameters A-F define the density profile; the radial factor B can also be a function of the latitude through the elongation parameter C ; A is the equatorial enhancement parameter; the parameter F defines the flatness of the shell; and D and E are the symmetry transition parameters that describe the abruptness of the geometrical transition in the shell.

It should be specified that we only consider the bright ring-nebula for this model. No attempt has been made to model the nebular northern extension since it is faint in the infrared and not clearly resolved.

A purely spherical model cannot reproduce the observed morphology of the dust shell because there would be too much emission at the center of the ring with respect to the observations. A sphere with equatorial enhancement may be considered to reproduce the difference in intensity between the two cuts on the infrared image. To appear nearly circular with a clear central hole in projection, a spherical shell with equatorial enhancement must be seen at small inclination $\lesssim 30^\circ$, roughly through the poles. This scheme is in agreement with the observed global morphology. At very low inclination it is difficult to reproduce the large difference in intensity between the two cuts in an axisymmetric model like this one. On the other hand, by increasing the inclination too much a strongly elliptical ring would be seen, which is not observed. In addition to the equatorial enhancement, the structure appears clumpy. These inhomogeneities cannot be reproduced by the present model. The best approximate axisymmetric model for the observed ring is a sphere with equatorial enhancement ($A \sim 5$) that is seen at small inclination ($\sim 30^\circ$). The values for the other five geometric parameters of Eq. (1) are $B = 3$, $C = 0$, $D = 0$, $E = 0$, $F = 1$ to keep the model simple and limit the number of free parameters.

The synthetic image produced by 2-Dust and convolved with the PACS PSF is given in the top right panel of Fig. 4. By comparing the PACS image to the synthetic one, we determined the inner, $r_{\text{in}} = 14''$, and the outer, $r_{\text{out}} = 42''$, radii of the dust ring. In the bottom panel of Fig. 4, cuts with PA = 160° and 70° through the central part of the observed and the simulated nebula are illustrated. Although the basic morphology (radii, thickness and axisymmetry of the shell) reproduced by the model agrees with the observed one, the intensity of the peaks does not because no attempt was made to fit the clumps, as mentioned earlier.

After constraining the nebular geometry we can proceed with the model of the dust SED. For the stellar parameters we adopted the distance $D = 6 \text{ kpc}$, the luminosity $\log L/L_\odot = 6.1$, and the temperature $T_{\text{eff}} = 20\,000 \text{ K}$ (Voors et al. 2000; Groh et al. 2009). The infrared SED of AG Car (Fig. 5) is too broad to be reproduced with only one population of dust grains, so we considered two populations of grains with the same composition but different sizes. Voors et al. (2000) showed that the dust in this nebula contains large grains, up to $40 \mu\text{m}$ in radius, and is dominated by amorphous silicates with little contribution from crystalline species, and more specifically pyroxenes with a 50/50 Fe to Mg abundance. We therefore adopted a similar dust composition. The optical constants of silicates given by Dorschner et al. (1995) were used for both populations, extrapolated to a constant refraction index in the far-ultraviolet. The size distribution for the dust grains of Mathis et al. (1977, hereafter MRN) was assumed, for each of the two populations: $n(a) \propto a^{-3.5}$ with $a_{\min} < a < a_{\max}$, where a is the grain radius. The model can be adjusted to the data by varying a_{\max} (or a_{\min}), which controls the $20 \mu\text{m}/100 \mu\text{m}$ flux density ratio, and the opacity, which controls the strength of the emission.

The best fit (Fig. 5) was achieved with the use of the following populations of dust grains. The first is a population of small grains with radii from 0.005 to $1 \mu\text{m}$, which is responsible for the emission at $\lambda < 40 \mu\text{m}$. The second is a population of large grains with radii from 1 to $50 \mu\text{m}$, which is responsible for the slope of the SED at $\lambda > 70 \mu\text{m}$. It should be pointed out that the large grains are necessary to reproduce the observed infrared SED. Several attempts were made to fit the SED using different grain sizes. They showed that a_{\max} cannot be very different from $50 \mu\text{m}$ for the population of large grains. More details are given in Appendix A.

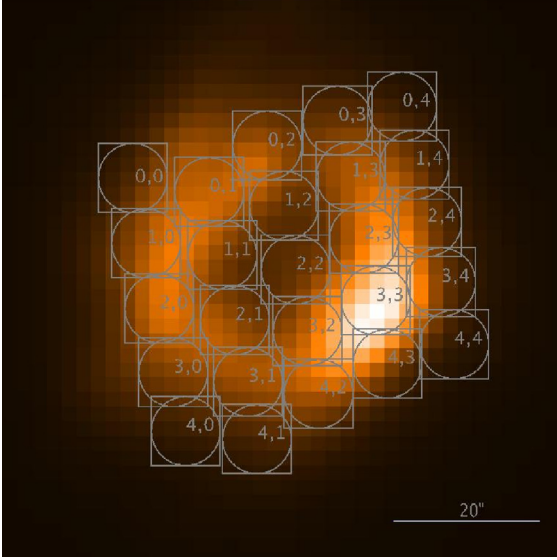


Fig. 6. Footprint of the PACS spectral field of view on the image of the AG Car nebula at $70\ \mu\text{m}$. Each number pair is the label of a specific spaxel. North is up and east is to the left.

The total mass of dust derived from the modeling is $M_{\text{dust}} \sim 0.21 M_{\odot}$ ($0.05 M_{\odot}$ from the small dust grains and $0.16 M_{\odot}$ from the large ones), with an uncertainty of $\sim 20\%$. This result is in agreement with the total dust mass found by Voors et al. (2000). The small grains have temperatures from 88 K at r_{in} to 62 K at r_{out} , while the large grains have temperatures from 43 K at r_{in} to 29 K at r_{out} . Similar results are obtained when fitting modified blackbody (BB) curves to the SED (see Appendix B for details).

As described in the introduction, AG Car is a variable star with photometric and spectroscopic variations. Although the data used for the dust model are obtained at different epochs, the visual magnitude of the star is approximately the same at the epochs of the IRAS, ISO, AKARI, and *Herschel* observations. In addition, AG Car varies under a roughly constant bolometric luminosity (Sect. 1). By keeping the luminosity constant and changing the radius and the temperature of the star within reasonable limits, we do not see significant changes in the model results.

5. Emission line spectrum

5.1. Spectrum overview

Figure 6 illustrates the footprint of the PACS spectral field of view on the image of the nebula at $70\ \mu\text{m}$. This field of view is composed of 25 (5×5) spaxels, each corresponding to a different part of the nebula, but it is not large enough to cover the whole nebula.

The integrated spectrum of the nebula over the 25 spaxels is shown in Fig. 7. Below $55\ \mu\text{m}$ the shape of the continuum results from a spectral response correction in this range that has not yet been perfected, while above $190\ \mu\text{m}$ it results from a light leak from the second diffraction order of the grating to the first one.

The following forbidden emission spectral lines are detected on the dust continuum: [OI] $\lambda\lambda$ 63, 146 μm , [N II] $\lambda\lambda$ 122, 205 μm , and [C II] λ 158 μm . The absence of higher ionization lines indicates that the ionization state of the gas in the nebula around AG Car is not as high as in the case of the nebulae around

other LBVs, for example WRAY 15-751 (Vamvatira-Nakou et al. 2013). This implies that the gas temperature is lower.

5.2. Line flux measurements

A Gaussian fit was performed on the line profiles to measure the emission line intensities in each of the 25 spectra (Fig. 6) using the Image Reduction and Analysis Facility (IRAF, Tody 1986,1993). The table with these measurements is given in Appendix C. We note that not all the lines are detected in the outer spaxels and that all fluxes reach their highest values at the spaxel (3,3). This spaxel corresponds to the southwestern part of the nebula, which is the brightest part (see Sect. 3).

Maps of the line intensities were created for each of the five detected lines in an effort to investigate whether there are differences in the gas properties for distinct parts of the nebula. There are only 25 spaxels, and the coverage of the nebula is not complete, so we cannot really see the full nebula in these “spectroscopic images”. The only wavelength at which we barely see the nebular ring is that of $122\ \mu\text{m}$. Furthermore, maps of line intensity ratios of every detected line to the [N II] $122\ \mu\text{m}$ line were created. The differences between distinct nebular regions are not significant or convincing. Since these maps are difficult to interpret given the large uncertainties on the fluxes and the wavelength-dependent PSF, they were not considered in the present study.

To measure the total flux of the nebula in each line we need to use the integrated spectrum over the 25 spaxels, but as already mentioned above the beam size of the PACS spectrometer is smaller than the size of the nebula. Consequently, the fluxes measured using the sum of the 25 spaxels do not correspond to the real nebular fluxes. For this reason, the PACS spectrum was corrected using the three PACS photometric observations. A modified BB was fitted to these data and another one to the continuum of the PACS spectrum, for wavelengths smaller than $190\ \mu\text{m}$. The ratio of the two curves gives the correction factor. In other words, the spectrum was scaled to the photometry. This factor linearly depends on the wavelength and goes from 1.11 at $55\ \mu\text{m}$ to 2.12 at $185\ \mu\text{m}$. This correction assumes a constant line-to-continuum ratio and is analogous to the point source correction applied in the pipeline to correct the effect of flux lost for a point source.

The [N II] $205\ \mu\text{m}$ line has a problematic calibration in PACS. Consequently, its flux needs to be corrected before being used in the following analysis. More precisely, the flux in [N II] $205\ \mu\text{m}$ is incorrect for all PACS measurements owing to a light leak, superimposing a lot of flux from $102.5\ \mu\text{m}$ at that wavelength. The relative spectral response function (RSRF) used to reduce the data suffers from the same light leak. Consequently, when this RSRF is applied during the data reduction, the signal at wavelengths $\geq 190\ \mu\text{m}$ is divided by a number that is too high. The continuum at these wavelengths is irremediably lost, but provided one can “scale-back up” with the right number to compensate for the exaggerated RSRF, one can recover the line-flux.

Using instrument test data obtained on the ground with calibration light sources set at different and known temperatures, one can invert the problem and reconstruct the “clean” RSRF, i.e., in the absence of light leak. This suffers from some defects and a large uncertainty due to the propagation of errors and to the very low response of the instrument at these wavelengths. A correction factor could nevertheless be derived from it, and confirmed within a certain margin by comparison of the line fluxes obtained for a few sources by both PACS and SPIRE at that wavelength. We finally found that the measured [N II] $205\ \mu\text{m}$

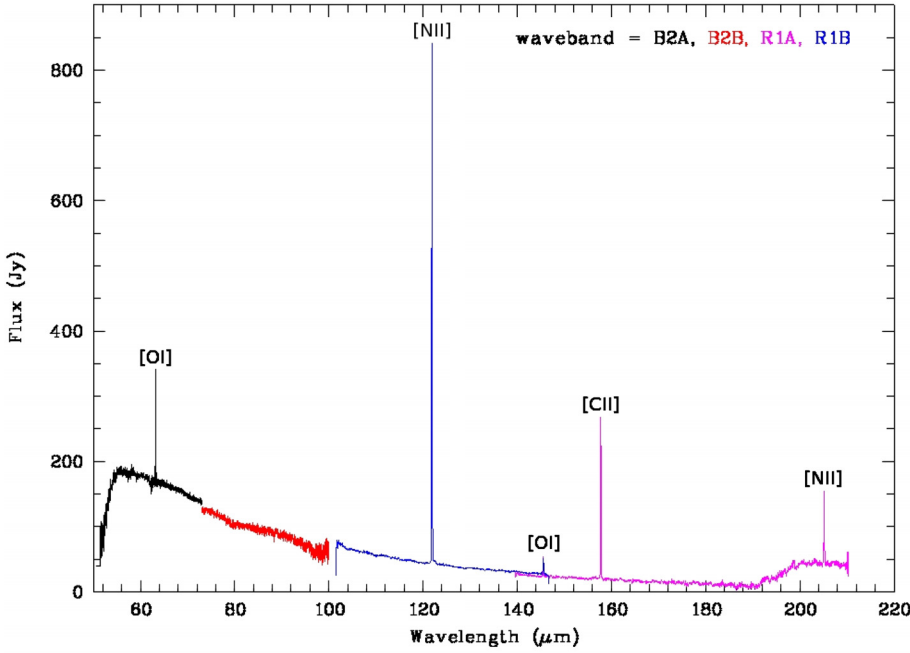


Fig. 7. PACS spectrum of the nebula around AG Car, integrated over the 25 spaxels. Indicated are the lines [OI], [NII], and [CII]. Below $55 \mu\text{m}$ the shape of the continuum results from a spectral response function correction that has not yet been perfected. Above $190 \mu\text{m}$ the shape results from a light leak from the second diffraction order of the grating in the first one. The different observing bands are indicated with different colors. We note that the spectral resolution depends on the waveband.

Table 2. Line fluxes of the nebula around AG Car.

Ion	λ (μm)	F (25 spaxels) ($10^{-15} \text{ W m}^{-2}$)	cf.	F (corrected) ($10^{-15} \text{ W m}^{-2}$)
[O I]	63	7.7	1.17	9.0 ± 1.8
[N II]	122	23.6	1.64	38.7 ± 7.7
[O I]	146	0.6	1.83	1.1 ± 0.3
[C II]	158	4.1	1.92	7.9 ± 1.6
[N II]	205	1.1	$2.26^a \times 4.2^b$	10.3 ± 2.6

Notes. ^(a) Missing flux correction ; ^(b) PACS/SPIRE cross-calibration factor.

flux should be multiplied by a correction factor of 4.2. An error of 25% was assumed for the final corrected [N II] $205 \mu\text{m}$ flux².

The emission line measurements of the nebula integrated over the 25 spaxels, before and after the correction for the missing flux, are given in Table 2 along with the correction factor (cf.) at each wavelength. It should be mentioned that the flux measurements of the three lines present in the ISO-LWS spectrum of AG Car ([O I] $\lambda 63 \mu\text{m}$, [N II] $\lambda 122 \mu\text{m}$ and [C II] $\lambda 158 \mu\text{m}$) do agree with the corrected values from the PACS spectrum within the errors, showing that the correction for the missing flux is essentially correct.

5.3. Photoionization region characteristics

The detected emission lines [N II] 122, $205 \mu\text{m}$ are associated with the H II region of the nebula around AG Car. The other three detected emission lines originate from a region of tran-

² This part of the infrared spectrum of AG Car has also been observed with SPIRE as part of the MESS program. Unfortunately, these data cannot be used so as to have a more precise flux for the line [N II] $205 \mu\text{m}$ because the whole ring nebula is outside of the detector coverage owing to the geometry of the detector array and because the observing mode was a single pointing and not a raster map. Consequently, any attempt to recover the nebular flux has huge uncertainty and we decided not to include the SPIRE spectroscopic data in our study.

sition between ionized and neutral hydrogen and may indicate the presence of a photodissociation region (PDR). Their analysis is given in the next subsection.

5.3.1. H α flux

The H α + [N II] flux from the nebula was estimated by integrating the surface brightness over the whole nebula. Contamination by field stars and the background was corrected and the emission from the occulted central part extrapolated. The continuum flux from the reflection nebula was measured in the adjacent filter, accounting for the difference in filter transmissions. However since AG Car is a strong emission-line star, the reflected stellar H α must also be subtracted. Considering the H α equivalent widths measured by Schulte-Ladbeck et al. (1994) and Stahl et al. (2001) for AG Car in 1993–1994 (i.e., accounting for ~ 1.5 years of time-delay) we estimate the final contamination due to the reflection nebula to be 20%. The contribution of the strong [N II] lines was then subtracted using the [N II]/H α ratios from available spectroscopic data and the transmission curve of the H α + [N II] filter. The conversion to absolute flux was done with the help of the three spectrophotometric standard stars and three planetary nebulae observed in the same filter; the conversion factors derived from these six objects show excellent internal agreement.

We measured $F_0(\text{H}\alpha) = 1.1 \times 10^{-10} \text{ erg cm}^{-2} \text{ s}^{-1}$ uncorrected for reddening. The uncertainty amounts to $\sim 20\%$. Adopting $E(B - V) = 0.59 \pm 0.03$ (de Freitas Pacheco et al. 1992), we derived $F_0(\text{H}\alpha) = 4.2 \pm 0.9 \times 10^{-10} \text{ erg cm}^{-2} \text{ s}^{-1}$ for the AG Car nebula. This flux is higher by a factor of 2 than the fluxes measured by Stahl (1987), Nota et al. (1992) and de Freitas Pacheco et al. (1992) in 1986, 1989, and 1991, but is compatible with the H β flux measured by Perek (1971) in 1969 (i.e., $F_0(\text{H}\alpha) \approx 3 \times 10^{-10} \text{ erg cm}^{-2} \text{ s}^{-1}$ with H α /H β = 6 and $E(B - V) = 0.59$). The flux density from the reflection nebula is $F_\lambda = 3.9 \times 10^{-13} \text{ erg cm}^{-2} \text{ s}^{-1} \text{ \AA}^{-1}$ at 6650 \AA (the central wavelength of the continuum filter). The high value of $F_0(\text{H}\alpha)$ we find is in agreement with the radio flux, also observed in 1994–1995 (Duncan & White 2002), and $E(B - V) = 0.59$.

5.3.2. Electron density

Smith et al. (1997) found a non-constant nebular electron density, n_e , that varies from 600 to 1050 cm^{-3} using the optical [S II] 6731/6717 ratio as an electron density diagnostic. Their result is in agreement with those of Mitra & Dufour (1990) and Nota et al. (1992) who used the same ratio as a diagnostic.

In the infrared waveband, the [N II] 122/205 μm ratio is a diagnostic for the electron density of the nebula at low density, $1 \text{ cm}^{-3} \leq n_e \leq 10^3 \text{ cm}^{-3}$ (Rubin et al. 1994). Considering the values of Table 2, this ratio is equal to 3.8 ± 1.2 for the whole nebula. The package *nebular* of the IRAF/STSDAS environment (Shaw & Dufour 1995) was used for the calculation of the electron density. An electron temperature, T_e , constant throughout the nebula and equal to $6350 \pm 400 \text{ K}$ was used for all of the following calculations. This is the average temperature calculated by Smith et al. (1997). The electron density is then found to be $160 \pm 90 \text{ cm}^{-3}$.

The calculated electron density based on the infrared data is much lower than the density based on the optical data. This discrepancy is usual and has also been observed in planetary nebulae (Liu et al. 2001; Tsamis et al. 2003). When the density of a nebula is spatially inhomogeneous, different line ratios used as density diagnostics lead to different values of the density. This is related to the difference in the critical density between the lines taken into consideration for the density calculation (Rubin 1989; Liu et al. 2001). The lines [N II] 122, 205 μm have lower critical densities than the lines [S II] 6731, 6717 \AA , which means that the calculated density using the first pair of lines is smaller than the density using the second pair (Rubin 1989).

In the following calculations we will use our estimate of the electron density based on infrared data because the electron density is best determined when it is similar to the critical density of the lines whose ratio is used as a diagnostic (Rubin et al. 1994). Otherwise, any attempt to calculate ionic abundances will give incorrect results (Rubin 1989; Liu et al. 2001).

5.3.3. Ionizing flux

To calculate the radius of the Strömgren sphere, R_S , and the rate of emission of hydrogen-ionizing photons, Q_0 , a steady nonvariable star must be considered. Such an analysis can be done in the case of a variable star like AG Car if the recombination time is longer than the variability timescale of the ionizing star. The recombination time is given by $\tau_{\text{rec}} = 1/n_e\alpha_B \text{ yr}$ (Draine 2011), where α_B is the recombination coefficient. Using the adopted value for the electron density and the assumed electron temperature, the recombination time was estimated to be about 520 yr. It is much longer than the timescale of the variability (5–10 yr) exhibited by the central star of the nebula, and this conclusion still holds if the higher electron density derived in the optical is considered. Therefore, an average nonvariable star is a valid approximation in our case.

The values of Q_0 and R_S can be determined first by using the estimated $H\alpha$ flux and second by using the radio flux density, $S_\nu = 268.7 \text{ mJy}$ at 6 cm (4.9 GHz) that was measured by Duncan & White (2002), adopting a typical error of 0.5 mJy. At 4.9 GHz the nebula is optically thin and it is assumed to be spherical with a uniform density.

The R_S in pc is given by (Vamvatira-Nakou et al. 2013)

$$R_S = 3.17 \left(\frac{x_e}{\epsilon} \right)^{1/3} \left(\frac{n_e}{100} \right)^{-2/3} T_4^{(0.272+0.007\ln T_4)} \left(\frac{Q_0}{10^{49}} \right)^{1/3}, \quad (2)$$

where Q_0 (in photons s^{-1}) using the $H\alpha$ flux is given by

$$Q_{0(H\alpha)} = 8.59 \times 10^{55} T_4^{(0.126+0.01\ln T_4)} D^2 F_0(H\alpha); \quad (3)$$

when using the radio flux it is given by

$$Q_{0(\text{radio})} = 8.72 \times 10^{43} T_4^{(-0.466-0.0208\ln T_4)} \left(\frac{\nu}{4.9} \right)^{0.1} x_e^{-1} D^2 S_\nu, \quad (4)$$

where $x_e = n_e/n_p$ is the ratio of the electron to the proton density, ϵ is the filling factor, $T_4 = T_e/(10^4 \text{ K})$, ν is the radio frequency in GHz, D is the distance of the nebula in kpc, $F_0(H\alpha)$ is the $H\alpha$ flux in $\text{erg cm}^{-2} \text{ s}^{-1}$, and S_ν is the radio flux in mJy.

Assuming $x_e = 1$ because the star is not hot enough to significantly ionize He and $T_4 = 0.635$, we found that the rate of emission of hydrogen-ionizing photons is $Q_{0(H\alpha)} = (1.2 \pm 0.5) \times 10^{48} \text{ photons s}^{-1}$ and $Q_{0(\text{radio})} = (1.0 \pm 0.4) \times 10^{48} \text{ photons s}^{-1}$. There is a good agreement between these two results within the uncertainties implying that the value of $E(B - V)$ adopted for the calculations is essentially correct. The mean value $Q_0 = (1.1 \pm 0.3) \times 10^{48} \text{ photons s}^{-1}$ corresponds to an early-B star with $T_{\text{eff}} \sim 26000 \text{ K}$ (Panagia 1973), which can be considered as the average spectral type of the star.

We also derived $R_S = 1.1 \pm 0.4 \text{ pc}$ assuming $\epsilon = 1$, i.e., that the ionized gas fills the whole volume of the nebula. The fact that the nebula is a shell and not a sphere, with inner radius of about $R_{\text{in}} = 11'' = 0.3 \text{ pc}$ in $H\alpha$, does not change this result because in that case the new Strömgren radius is $R'_S = (R_S^3 + R_{\text{in}}^3)^{1/3} = 1.1 \text{ pc}$. The Strömgren radius is the radius of an ionization bounded nebula by definition. In Sect. 3, it was observed that the faint part of the nebula in $H\alpha$ extends up to 0.7 pc from the central star. Moreover, the northern faint extension discussed in that section extends up to 1 pc. The comparison of these numbers with the estimated value of the Strömgren radius, considering the uncertainties, leads to the conclusion that the $H\alpha$ nebula may be ionization bounded. The presence of PDR signatures in the spectrum supports this conclusion. This value of the Strömgren radius is only an average value which can vary locally depending on the density inhomogeneities. In particular, according to the adopted morphological model, the electron density of the shell could be higher along the equator and smaller along the poles so that the ionizing radiation can reach the faint extensions or bipolar lobes.

5.3.4. Abundance ratio N/H

Given the detected emission lines in the spectrum and the lack of [N III] 57 μm and [O III] 88 μm , only an estimate of the N/H abundance number ratio can be made based on the observed $H\alpha$ 6562.8 \AA , [N II] 122 μm and 205 μm lines and considering that

$$\frac{N}{H} = \frac{\langle N^+ \rangle}{\langle H^+ \rangle}. \quad (5)$$

The flux ratios $F/F_0(H\beta)$ were calculated for the two infrared lines of [N II] with the observed values of F from Table 2. Using the dereddened $H\alpha$ flux, a case-B recombination with $T_e = 6350 \text{ K}$ was assumed to calculate the $H\beta$ flux, adopting the effective recombination coefficient equations of Draine (2011). The ionic abundances N^+/H^+ were then derived using the package *nebular*. The N/H abundance number ratio was calculated to be $(2.6 \pm 1.2) \times 10^{-4}$, which is equivalent to a logarithmic value of $12 + \log(N/H) = 8.41 \pm 0.20$. Considering the errors, this value is entirely compatible with that of Smith et al. (1997), which is 8.27 ± 0.05 . It is significantly higher than the solar value (7.83, Grevesse et al. 2010).

5.3.5. Mass of the ionized gas

An estimate of the ionized gas mass can be made from the $H\alpha$ and the radio emissions. The equations that are analytically derived in Vamvatira-Nakou et al. (2013) are used for this calculation.

For a spherical nebula the ionized mass in solar masses, taking into account the $H\alpha$ emission, is given by

$$M_{i(H\alpha)}^{\text{sphere}} = 57.9 \frac{1 + 4y_+}{\sqrt{1 + y_+}} T_4^{(0.471 + 0.015 \ln T_4)} \epsilon^{1/2} \theta^{3/2} D^{5/2} F_0^{1/2} (H\alpha), \quad (6)$$

where θ is the angular radius of the nebula ($R = \theta D$) in arcsec and $n_{H^+} = n_p$, n_{He^+} , and $n_{He^{++}}$ are the number densities of the ionized hydrogen, ionized helium, and doubly ionized helium, respectively. Assuming $n_{He^{++}} = 0$ and denoting $y_+ = n_{He^+}/n_{H^+}$, we have $x_e = n_e/n_p \simeq 1 + n_{He^+}/n_{H^+} = 1 + y_+$ and $\mu_+ \simeq 1 + 4 n_{He^+}/n_{H^+} = 1 + 4y_+$.

Considering now the radio flux and using the same formalism as above, the mass of a spherical nebula in solar masses is given by

$$M_{i(\text{radio})}^{\text{sphere}} = 5.82 \times 10^{-5} \frac{1 + 4y_+}{1 + y_+} T_4^{0.175} \left(\frac{\nu}{4.9} \right)^{0.05} \epsilon^{1/2} \theta^{3/2} D^{5/2} S_\nu^{1/2}. \quad (7)$$

In $H\alpha$ the nebula around AG Car is a shell with inner radius $\theta_{\text{in}} = 11''$ and an average outer radius $\theta_{\text{out}} = 20''$. In the radio the nebula has approximately the same radii (Duncan & White 2002). In this case the mass of the ionized shell nebula is given by

$$M_i^{\text{shell}} = (\theta_{\text{out}}^3 - \theta_{\text{in}}^3)^{1/2} \theta_{\text{out}}^{-3/2} M_i^{\text{sphere}}. \quad (8)$$

The mass of the ionized shell nebula is thus $M_{i(H\alpha)}^{\text{shell}} = 6.9 \pm 2.8 M_\odot$ and $M_{i(\text{radio})}^{\text{shell}} = 6.4 \pm 2.5 M_\odot$, with an average value of $M_i^{\text{shell}} = 6.6 \pm 1.9 M_\odot$, assuming $\epsilon = 1$. The assumption that the ionization of He is negligible ($y_+ = 0$) was made because the central star has a temperature lower than 30 000 K. This result is slightly higher, considering the uncertainties, than the mass of $4.2 M_\odot$ estimated by Nota et al. (1992, 1995).

5.4. Photodissociation region characteristics

The fine structure emission lines [O I] 63, 146 μm and [C II] 158 μm are among the most important coolants in PDRs (Hollenbach & Tielens 1997). Their detection in our spectrum may indicate the presence of a PDR in the nebula. On the other hand, a shock, which is the result of the interaction between the fast stellar wind and the slow expanding remnant of a previous evolutionary phase, could also photodissociate molecules and result in [O I] and [C II] emission. However, the values of the calculated ratios of [O I] 63 μm /[O I] 146 μm and [O I] 63 μm /[C II] 158 μm are in agreement with the PDR models of Kaufman et al. (1999) and not with the shock models of Hollenbach and McKee (1989). In particular, the ratio [O I] 63 μm /[C II] 158 μm is a diagnostic between PDR and shock as it is < 10 in PDRs (Tielens & Hollenbach 1985). Consequently, based on these ratios, we can conclude that a PDR and not a shock is present in the nebula around the LBV AG Car and that it is responsible for the [O I] and [C II] emission. Photodissociation regions were detected in the nebula that surrounds the LBV HR Car (Umana et al. 2009) and in the nebula around the LBV candidate HD 168625 (Umana et al. 2010). Later on, the infrared study of

the LBV WRAY 15-751 also revealed the presence of a PDR in the nebula that surrounds this star (Vamvatira-Nakou et al. 2013).

The physical conditions in the PDR can be determined using these three infrared lines, but because of the vicinity of the bright Carina nebula, we have to check if these lines come entirely from the LBV nebula or if there is a significant contribution to the measured fluxes from the background. We therefore checked the spectra of the background taken at two different positions on the sky and found that the lines [O I] 63 μm , 146 μm come entirely from the nebula. However, the flux of the line [C II] 158 μm is contaminated by the [C II] foreground/background emission. For the nebular spectrum discussed and analyzed in this section, the background has been subtracted, as mentioned in Sect. 2. Nevertheless, careful examination of the two off-source spectra shows that the background is strong and not uniform. The difference between the spectra of the two off positions induces an uncertainty of at least a factor of 2 on the [C II] 158 μm line flux. Hence, the measured [C II] 158 μm flux is unreliable and the mass of hydrogen in the PDR based on the [C II] flux cannot be estimated. We note that the previous conclusion about the presence of a PDR in the nebula is still valid when background contamination is taken into account.

The structure of the PDR is described by the density of the atomic hydrogen, n_{H^0} , and the incident FUV radiation field, G_0 , which can be calculated using the following equation (Tielens 2005), where it is expressed in terms of the average interstellar radiation field that corresponds to an unidirectional radiation field of $1.6 \times 10^{-3} \text{ erg cm}^{-2} \text{ s}^{-1}$,

$$G_0 = 625 \frac{L_\star \chi}{4\pi R^2}, \quad (9)$$

where L_\star is the stellar luminosity, χ is the fraction of this luminosity above 6 eV, which is ~ 0.7 for an early-B star (Young Owl et al. 2002), and R is the distance from the star. For the PDR of the AG Car nebula, the incident FUV radiation field is then $G_0 \simeq 3.7 \times 10^4$, considering that $L_\star = 10^{6.1} L_\odot$ (Sect. 4) and $R = 0.7 \text{ pc}$, which is the radius of the ionized gas region surrounded by the PDR. This result can be used to constrain the density of the PDR. The diagnostic diagram of the PDR models of Kaufman et al. (1999, Figs. 4 and 5) give the ratios of the fluxes $F_{[O I]63}/F_{[C II]158}$ and $F_{[O I]145}/F_{[O I]63}$ as a function of the density and the incident FUV radiation field. By using only the latter ratio and the calculated G_0 and considering the uncertainties, we can estimate the density of the PDR to be $\log n_{H^0} \simeq 3$, with a large uncertainty.

To verify the consistency of the PDR analysis with the results of the dust nebula analysis, the dust temperature, T_{dust} , can be estimated based on the radiative equilibrium, since the dust absorbs and re-emits the FUV radiation in the far-infrared. In case of silicates (i.e., $\beta = 2$) the dust temperature is given by (Tielens 2005)

$$T_{\text{dust}} = 50 \left(\frac{1 \mu\text{m}}{a} \right)^{0.06} \left(\frac{G_0}{10^4} \right)^{1/6} \text{ K for } T_{\text{dust}} < 250 \text{ K}. \quad (10)$$

We obtain a dust temperature of $T_{\text{dust}} = 71 \text{ K}$, assuming a typical grain size of $a = 0.1 \mu\text{m}$ because the average cross-section is dominated by small grains. This result is in agreement with the results of the 2-Dust model (Sect. 4).

6. Discussion

The parameters of the LBV AG Car given in Table 3 summarize the measurements obtained in this work along with results taken

Table 3. Parameters of the LBV AG Car and its shell nebula.

Star	$\log L/L_{\odot}$	6.1 ± 0.2
	T_{eff} (K)	$20\,000 \pm 3000$
	D (kpc)	6.0 ± 1.0
Shell	r_{in} (pc)	0.4
	r_{out} (pc)	1.2
	v_{exp} (km s ⁻¹)	70
	t_{kin} (10 ⁴ yr)	1.7
	n_e (cm ⁻³)	160 ± 90
	T_e (K)	6350 ± 400
	N/O	5.7 ± 2.2
	12+log N/H	8.41 ± 0.20
	M_{dust} (M_{\odot})	0.20 ± 0.05
	$M_{\text{ion,gas}}$ (M_{\odot})	6.6 ± 1.9

from previous studies. The stellar parameters of luminosity, effective temperature, and distance are from Voors et al. (2000), Groh et al. (2009), Humphreys et al. (1989), and this work. The parameters for the shell include the radii, the expansion velocity (Smith 1991), the kinematic age, the ionized gas electron density and the adopted electron temperature, the abundance ratios (N/O from Smith et al. (1997) and N/H from our study), and the measured masses of dust and gas.

The *Herschel*-PACS infrared images of the LBV AG Car reveal a dusty shell nebula that surrounds the central star. It is a clumpy ring with an inner radius of 0.4 pc and an outer radius of 1.2 pc. The $H\alpha + [\text{N II}]$ images show a gas shell nebula that coincides with the dust nebula, but seems to be slightly smaller and more elliptical. The nebula has bipolar morphology, a common feature among LBV nebulae (Weis 2001; Lamers et al. 2001).

The nebula around AG Car lies in an empty cavity (Fig. 3). If associated with the star, the cavity may correspond to a previous mass-loss event when the wind of the O-type progenitor formed a bubble, as in the case of WR stars (Marston 1996). A similar case is the cavity observed around the LBV WRAY 15-751 (Vamvatira-Nakou et al. 2013), though the latter is much larger. Velocity mapping of the surrounding interstellar gas would be needed to confirm this hypothesis and derive constraints on the O-star evolutionary phase.

The results of our study point to a shell nebula of ionized gas and dust, surrounded by a thin photodissociation region that is heated by an average early-B star. The dust mass-loss rate is about $(1.8 \pm 0.5) \times 10^{-5} M_{\odot} \text{ yr}^{-1}$, considering the duration of the enhanced mass-loss episode that was estimated from the kinematic age of the inner and outer radii of the nebula. Because we do not know the total gas mass as we cannot calculate the neutral gas mass, we must assume a gas-to-dust mass ratio in order to estimate the total mass-loss rate. A typical value for this ratio is 100 and so the gas mass will be $\sim 20 M_{\odot}$. In the study of the nebula around the LBV WRAY 15-751 (Vamvatira-Nakou et al. 2013), this ratio was calculated to be about 40. If we assume a similar value, the gas mass will be about $10 M_{\odot}$, higher than but comparable to the mass of the ionized gas. Adopting the average value, the gas mass of the nebula around AG Car is about $15 M_{\odot}$ with an uncertainty of about 30%. The total mass-loss rate is then estimated to be $(1.4 \pm 0.5) \times 10^{-3} M_{\odot} \text{ yr}^{-1}$.

It is interesting to compare this mass-loss rate that corresponds to the period during which the ejection took place with recent mass-loss rates. Leitherer et al. (1994) found $\dot{M}(\text{H}) = 0.6 \times 10^{-5}$ to $4.0 \times 10^{-5} M_{\odot} \text{ yr}^{-1}$ in 1990–1992 when the star luminosity was rising, showing no significant dependence on the luminosity phase. Groh et al. (2009) studied the fundamental parameters of AG Car during the last two periods of minimum,

1985–1990 and 2000–2003, and calculated a mass-loss rate from 1.5×10^{-5} to $6.0 \times 10^{-5} M_{\odot} \text{ yr}^{-1}$. The mass-loss rate during the nebula ejection phase thus appears roughly 50 times higher than in the present evolutionary phase.

The N/O ratio of 5.7 ± 2.2 calculated by Smith et al. (1997) points to the presence of highly processed material because it is much higher than the solar abundances. It is the highest value of N/O among the known LBVs, except the case of η Car (Smith et al. 1998). The 12+log N/H abundance of 8.41 ± 0.20 , calculated on the basis of our observations, is enhanced by a factor of 4.3 with respect to the solar abundance. It is lower than the value for the LBV η Car and higher than the values reported for all other LBVs (Smith et al. 1998).

Groh et al. (2009) calculated the surface abundances of several chemical elements at the surface of the star. The comparison of the nebular abundances with the surface ones shows that the N/O abundance ratio of the nebula is much lower than the surface value of 39^{+28}_{-18} . As the authors mention, this is compatible with the idea that the nebulae around massive stars contain material that is less processed than the material of the stellar photosphere.

Smith et al. (1997), based on a detailed abundances study, argued that the AG Car nebula was formed from material ejected during a RSG phase. This was also the suggestion of Voors et al. (2000) based on their analysis of the dusty nebula, but Lamers et al. (2001), in their study of the chemical composition of LBVs, concluded that the ejection occurred in a blue supergiant (BSG) phase as this can better explain the high expansion velocity. Moreover, the problem with an ejection during a RSG phase is the lack of luminous RSGs in the HR diagram.

Based on our observations as well as on evolutionary models (Ekström et al. 2012), we can constrain the evolutionary path of the central star and the epoch at which the nebula was ejected, using the abundance ratios, the measured mass-loss rate, and the timescale of the ejection as constraints. The only available abundance ratio that can be used is the N/O ratio. The N/H abundance ratio is indeed sensitive to inhomogeneities of the nebula (Lamers et al. 2001). It should also be stressed that the evolutionary models for massive stars are very uncertain at the post-main-sequence phases as they do not include any eruptive event, which means that the mass-loss rate recipes are poorly known (Smith 2014).

A constraint on the initial rotational velocity of AG Car can be imposed, based on the results of Groh et al. (2011). In their study of AG Car during two periods of visual minimum, they concluded that the progenitor did not have a high initial rotational velocity, although they measured the current projected rotational velocity to be 220 km s^{-1} . Their conclusions were based on the comparison with the evolutionary paths of Meynet & Maeder (2003). The luminosity and effective temperature of the star were found to be compatible with the evolutionary tracks of a nonrotating star with initial mass between 40 and $60 M_{\odot}$.

The total mass-loss rate, estimated during the nebular ejection, is quite high but uncertain. A lower limit of the mass-loss rate can be considered, based on the sum of the dust mass and the ionized gas mass that are well determined in the nebula ring. Considering the errors, this lower limit is $\log \dot{M} = -3.4$, where \dot{M} is in $M_{\odot} \text{ yr}^{-1}$. This result along with the nebular N/O abundance ratio, which is assumed to be the surface abundance ratio at the time of the ejection, were compared to the computed evolution of the mass-loss rate versus this abundance ratio using the models of Ekström et al. (2012) for stars of initial masses that correspond to the high stellar luminosity of AG Car, considering four different cases of stellar rotation from no rotation to a rotation rate of $\Omega/\Omega_{\text{crit}} = 0.4$. In Fig. 8, the evolution of

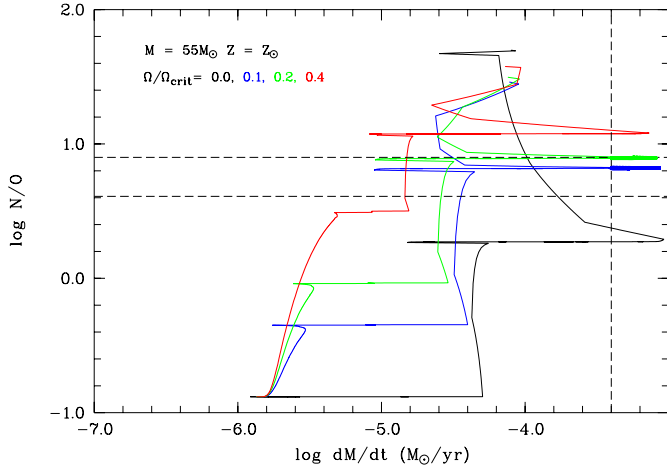


Fig. 8. Evolution of the N/O surface abundance ratio as a function of the mass-loss rate for a $55 M_{\odot}$ star of solar metallicity and for initial rotation rates $\Omega/\Omega_{\text{crit}}$ from 0 to 0.4, using the models of Ekström et al. (2012). The dashed lines correspond to the adopted value of N/O, with its errors, and the lower limit for the mass-loss rate. The thicker lines emphasize the part of the tracks compatible with the measurements. For clarity, the tracks are stopped during the He burning phase (data point n° 195 in Ekström et al. 2012).

the mass-loss ratio versus the N/O abundance ratio is illustrated for a $55 M_{\odot}$ star from the models of Ekström et al. (2012). The measured N/O value, with its errors, and the measured lower limit of the mass-loss rate are plotted with dashed lines. The part of these tracks compatible with the measurements is emphasized with thicker lines. To identify at which evolutionary phase of the star this corresponds, the same parts of the tracks are reported in the HR diagram (Fig. 9).

Our results are compatible with the evolutionary tracks of the models of Ekström et al. (2012) for a star of $55 M_{\odot}$ with solar metallicity and medium rotational velocity. In this case, the ejection of the nebula occurs in a post-main-sequence short-lived episode of high mass loss in agreement with the observations. We note that in such short-lived episodes, the mass-loss rate could be higher than computed from the model since the model does not account for eruptive events. For a star of $57 M_{\odot}$ the only compatible evolutionary track is the nonrotating one. Consequently, we can conclude that the star may have a low initial rotational velocity as suggested by Groh et al. (2011). For a mass of $50 M_{\odot}$, the only compatible evolutionary track is the one rotating at $\Omega/\Omega_{\text{crit}} = 0.4$. For a mass of $60 M_{\odot}$, the N/O ratio is reached on the main sequence where the mass-loss rate is much smaller than our lower limit, such that no track is compatible with both the observed N/O ratio and a short-lived ($\leq 2 \times 10^4$ yr) high mass-loss event.

A star with initial mass between 40 and $60 M_{\odot}$ immediately evolves to a BSG without passing through the RSG phase. It then evolves towards the LBV and the WR phase (Meynet et al. 2011). Groh et al. (2014) performed a detailed study on the evolutionary stages of a nonrotating star of $60 M_{\odot}$ with solar metallicity, combining the evolutionary models of Ekström et al. (2012) with atmospheric models. Before the WR phase, the evolutionary tracks of a $55 M_{\odot}$ star (Fig. 9) with little rotation are very similar to the track of Groh et al. (2014) for a $60 M_{\odot}$ without rotation in terms of effective temperature and luminosity. Making use of this result points to an ejection of the nebula during the LBV evolutionary phase of AG Car and more precisely during a cool LBV phase. Compared to the results ob-

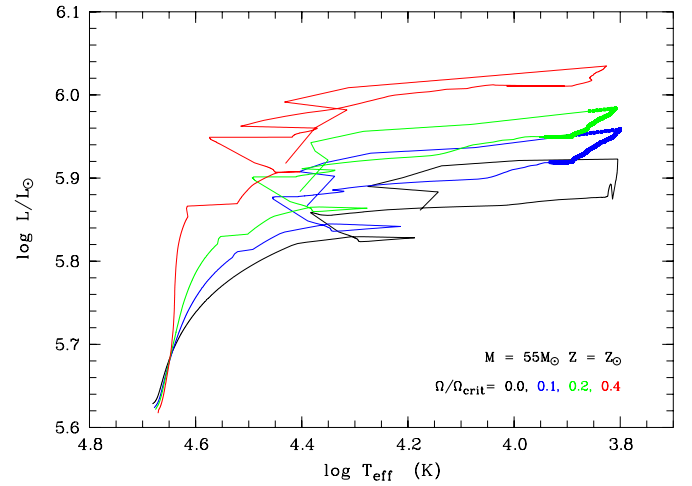


Fig. 9. Evolutionary path in the HR diagram of a $55 M_{\odot}$ star of solar metallicity and for initial rotation rates $\Omega/\Omega_{\text{crit}}$ from 0 to 0.4, using the models of Ekström et al. (2012). The thicker lines emphasize the part of the tracks compatible with the N/O abundance ratio and the mass-loss rate. For clarity, the tracks are stopped during the He burning phase (data point n° 195 in Ekström et al. 2012).

tained for WRAY 15-751, a lower luminosity LBV that passed through a RSG phase where the ejection of its nebula took place (Vamvatira-Nakou et al. 2013), this indicates that depending on their luminosity, LBV nebulae can be ejected at different evolutionary stages. It should be mentioned that de Freitas Pacheco et al. (1992) compared the AG Car nebular properties, based on their spectroscopic observations, with the evolutionary models available at that time, and concluded that they were consistent with the properties of a star of $60 M_{\odot}$ at the beginning of the LBV phase.

The model of the dust nebula in Sect. 4 showed that large dust grains are necessary to reproduce the observed infrared SED, in agreement with the results of Voors et al. (2000). This was also the case for the dust nebulae around the LBV WRAY 15-751 (Vamvatira-Nakou et al. 2013) and the yellow hypergiant Hen 3-1379, a possible pre-LBV (Hutsemékers et al. 2013). Large grains ($a > 5 \mu\text{m}$) have also been detected in supernovae (Gall et al. 2014). In the case of LBVs, the stellar temperature is most often too high for dust formation to take place so that dust production can only happen during large eruptions, when a pseudo-photosphere with a sufficiently low temperature is formed. As shown by Kochanek (2011, 2014), large dust grains can be produced during LBV eruptions and other transients when the conditions of high mass-loss rate and low pseudo-photosphere temperature are encountered. According to these models, to produce grains larger than $10 \mu\text{m}$, the central star should have gone through a great outburst, with a pseudo-photosphere temperature as low as 4000 K, i.e., much lower than during normal eruptions. During this event, the mass-loss rate is expected to be as high as $10^{-2} M_{\odot} \text{yr}^{-1}$. For AG Car, this would require a duration of the event shorter than estimated from the shell thickness, which is possible if the shell thickness is mostly due to a spread in velocity (Kochanek 2011).

7. Conclusions

The analysis of *Herschel* PACS imaging and spectroscopic observations of the nebula around the LBV AG Car, along with optical imaging data have been presented. The PACS images show

that the dust nebula appears as a clumpy ring. It coincides with the $H\alpha$ nebula, but extends farther out.

The determination of the dust parameters of the nebula was performed by dust modeling with the help of a two-dimensional radiative transfer code. This model points to the presence of both a small and a large grain population of pyroxenes with a 50/50 Fe to Mg abundance. Large grains ($a \gtrsim 10 \mu\text{m}$) are needed to reproduce the observational data.

The infrared spectrum of the nebula consists of forbidden emission lines over a dust continuum, without the presence of any other dust feature. These lines reveal the presence of ionized and photodissociation regions that are mixed with the dust. The derived gas abundances show a strong N/O and N/H enhancement as well as a O/H depletion, which is expected for massive evolved stars enriched with CNO-cycle processed material.

The evolutionary path of the star and the epoch at which the nebula was ejected were constrained using the abundances, mass-loss rate and available evolutionary models. The results point to a nebular ejection during a cool LBV evolutionary phase of a star with initial mass of about $55 M_{\odot}$ and with little rotation.

Acknowledgements. We thank the referee, Rens Waters, for his careful reading and his constructive suggestions that greatly improved the manuscript. C.V.N., D.H., P.R., N.L.J.C., Y.N. and M.A.T.G. acknowledge support from the Belgian Federal Science Policy Office via the PRODEX Programme of ESA. The Liège team also acknowledges support from the FRS-FNRS (Comm. Franç. de Belgique). PACS has been developed by a consortium of institutes led by MPE (Germany) and including UVIE (Austria); KU Leuven, CSL, IMEC (Belgium); CEA, LAM (France); MPIA (Germany); INAF-IFSI/OAA/OAP/OAT, LENS, SISSA (Italy); IAC (Spain). This development has been supported by the funding agencies BMVIT (Austria), ESA-PRODEX (Belgium), CEA/CNES (France), DLR (Germany), ASI/INAF (Italy), and CICYT/MCYT (Spain). Data presented in this paper were analyzed using “HIPE”, a joint development by the *Herschel* Science Ground Segment Consortium, consisting of ESA, the NASA *Herschel* Science Center, and the HIFI, PACS and SPIRE consortia. This research has made use of the NASA/IPAC Infrared Science Archive, which is operated by the Jet Propulsion Laboratory, California Institute of Technology, as well as NASA/ADS and SIMBAD (CDS/Strasbourg) databases.

References

- Beichman, C. A., Neugebauer, G., Habing, H. J., Clegg, P. E., & Chester, T. J. 1988, *Infrared Astronomical Satellite (IRAS) Catalogs and Atlases*, Vol. 1, Explanatory Supplement
- Bouret, J.-C., Lanz, T., & Hillier, D. J. 2005, *A&A*, **438**, 301
- Cannon, A. J. 1916, *Harvard Annals*, **76**, 19
- Conti, P. S. 1984, *IAUS*, **105**, 233
- Dorschner, J., Begemann, B., Henning, T., Jaeger, C., & Mutschke, H. 1995, *A&A*, **300**, 503
- Draine, B. T. 2011, *Physics of the Interstellar and Intergalactic Medium*, (Princeton University Press)
- Duncan, R. A., & White, S. M. 2002, *MNRAS*, **330**, 63
- Ekström, S., Georgy, C., Eggenberger, P., et al. 2012, *A&A*, **537**, A146
- de Freitas Pacheco, J. A., Damineli Neto, A., Costa, R. D. D., & Viotti, R. 1992, *A&A*, **266**, 360
- Fullerton, A. W., Massa, D. L., & Prinja, R. K. 2006, *ApJ*, **637**, 1025
- Gall, C., Hjorth, J., Watson, D., et al. 2014, *Nature*, **511**, 326
- Gravese, N., Asplund, M., Sauval, A. J., & Scott, P. 2010, *Ap&SS*, **328**, 179
- Griffin, M. J., Abergel, A., Abreu, A., et al. 2010, *A&A*, **518**, A3
- Groenewegen, M. A. T., Waelkens, C., Barlow, M. J., et al. 2011, *A&A*, **526**, A162
- Groh, J. H., Hillier, D. J., Damineli, A., et al. 2009, *ApJ*, **698**, 1698
- Groh, J. H., Hillier, D. J., Damineli, A. 2011, *ApJ*, **736**, 46
- Groh, J. H., Meynet, G., Ekström, S., & Georgy, C. 2014, *A&A*, **564**, A30
- Hildebrand, R. H. 1983, *QJRAS*, **24**, 267
- Hoekzema, N. M., Lamers, H. J. G. L. M., & van Genderen, A. M. 1992, *A&A*, **257**, 118
- Hollenbach, D., & McKee, C. F. 1989, *ApJ*, **342**, 306
- Hollenbach, D. J., & Tielens, A. G. G. M. 1997, *ARA&A*, **35**, 179
- Humphreys, R. M. 1989, in *Physics of luminous blue variables*, IAU Colloq. 113, eds. K. Davidson, A. F. J. Moffat, & H. J. G. L. M. Lamers (Canada: Val Morin), 3
- Humphreys, R. M., & Davidson, K. 1979, *ApJ*, **232**, 409
- Humphreys, R. M., & Davidson K. 1994, *PASP*, **106**, 1025
- Humphreys, R. M., Lamers, H. J. G. L. M., Hoekzema, N., & Cassatella, A. 1989, *A&A*, **218**, 17
- Hutsemékers, D. 1994, *A&A*, **281**, L81
- Hutsemékers, D. 1997, *ASPC*, **120**, 316
- Hutsemékers, D., Cox, N. L. J., Vamvatira-Nakou, C. 2013, *A&A*, **552**, L6
- Ishihara, D., Onaka, T., Kataza, H., et al. 2010, *A&A*, **514**, A1
- Jiménez-Esteban, F. M., Rizzo, J. R., & Palau, A. 2010, *ApJ*, **713**, 429
- Kaufman, M. J., Wolfire, M. G., Hollenbach, D. J., & Luhman, M. L. 1999, *ApJ*, **527**, 795
- Kessler, M. F., Steinz, J. A., Anderegg, M. E., et al. 1996, *A&A*, **315**, L27
- Kochanek, C. S. 2011, *ApJ*, **743**, 73
- Kochanek, C. S. 2014, *MNRAS*, submitted [[arXiv:1407.7856](https://arxiv.org/abs/1407.7856)]
- Lamers, H. J. G. L. M., Hoekzema, N., Trams, N. R., Cassatella, A., & Barylak, M. 1989, in *Physics of luminous blue variables*, IAU Colloq. 113, eds. K. Davidson, A. F. J. Moffat & H. J. G. L. M. Lamers (Canada: Val Morin), 271
- Lamers, H. J. G. L. M., Nota, A., Panagia, N., Smith, L. J., & Langer, N. 2001, *ApJ*, **551**, 764
- Leitherer, C., Damineli N. A., & Schmutz, W. 1992, *ASPC*, **22**, 366
- Leitherer, C., Allen, R., Altner, B., et al. 1994, *ApJ*, **428**, 292
- Liu, X.-W., Barlow, M. J., Cohen, M., et al. 2001, *MNRAS*, **323**, 343
- Lorente, R., Onaka, T., Ita, Y., et al. 2008, *AKARI IRC Data User Manual*
- Maeder, A., & Meynet, G. 2010, *New Astron. Rev.*, **54**, 32
- Marston, A. P. 1996, *AJ*, **112**, 2828
- Mathis, J. S., Rumpl, W., & Nordsieck, K. H. 1977, *ApJ*, **217**, 425
- McGregor P. J., Hyland A. R., & Hillier D. J. 1988, *ApJ*, **324**, 1071
- Meixner, M., Ueta, T., Bobrowsky, M., & Speck, A. 2002, *ApJ*, **571**, 936
- Melnick J., Dekker H., & D’Odorico S. 1989, *EFOSC*, ESO operating manual 4
- Meynet, G., & Maeder, A. 2003, *A&A*, **404**, 975
- Meynet, G., Georgy, C., Hirschi, R., et al. 2011, *Bull. Soc. Roy. Sci. Liège*, **80**, 266
- Mitra, P. M., & Dufour, R. J. 1990, *MNRAS*, **242**, 98
- Molinari, S., Swinyard, B., Bally, J., et al. 2010, *PASP*, **122**, 314
- Müller, T., Okumura K., & Klaas U. 2011, PACS Photometer Passbands and Colour Correction Factors for Various Source SEDs
- Murakami, H., Baba, H., Barthel, P., et al. 2007, *PASJ*, **59**, 369
- Neugebauer, G., Habing, H. J., van Duinen, R., et al. 1984, *ApJ*, **278**, 1
- Nota, A., Leitherer, C., Clampin, M., Greenfield, P., & Golimowski, D. A. 1992, *ApJ*, **398**, 621
- Nota, A., Livio M., Clampin M., & Schulte-Ladbeck R. 1995, *ApJ*, **448**, 788
- Nota, A., Clampin, M., Garcia-Segura, G., Leitherer, C., & Langer, N. 1996, in *Science with the Hubble Space Telescope: II*, eds. P. Benvenuti, F. D. Macchetto, & E. J. Schreier (Baltimore: STScI), 398
- Nota A., Pasquali A., Marston A. P., et al. 2002, *AJ*, **124**, 2920
- Ott, S. 2010, *ASP Conf. Ser.*, **434**, 139
- Panagia, N. 1973, *AJ*, **78**, 929
- Perek, L. 1971, *Bull. Astr. Inst. Czechosl.*, **22**, 103
- Paresce, F., & Nota, A. 1989, *ApJ*, **341**, 83
- Pilbratt, G. L., Riedinger, J. R., Passvogel, T., et al. 2010, *A&A*, **518**, L1
- Poglitsch, A., Waelkens, C., Geis, N., et al. 2010, *A&A*, **518**, L2
- Puls, J., Markova N., & Scuderi S. 2008, *ASPC*, **388**, 101
- Roussel, H. 2013, *PASP*, **125**, 1126
- Rubin, R. H. 1989, *ApJS*, **69**, 897
- Rubin, R. H., Simpson, J. P., Lord, S. D., et al. 1994, *ApJ*, **420**, 772
- Schulte-Ladbeck, R. E., Clayton, G. C., Hillier, D. J., Harries, T. J., & Howarth, I. D. 1994, *ApJ*, **429**, 846
- Shaw, R. A., & Dufour, R. J. 1995, *PASP*, **107**, 896S
- Smith, L. J. 1991, *IAUS*, **143**, 385
- Smith, L. J., Crowther, P. A., & Prinja, R. K. 1994, *A&A*, **281**, 833
- Smith, L. J., Stroud, M. P., Esteban, C., & Vilchez, J. M. 1997, *MNRAS*, **290**, 265
- Smith, L. J., Nota, A., Pasquali, A., et al. 1998, *ApJ*, **503**, 278
- Smith, N. 2014, *ARA&A*, **52**, 487
- Stahl, O. 1986, *A&A*, **164**, 321
- Stahl, O. 1987, *A&A*, **182**, 229
- Stahl, O., & Wolf, B. 1986, *A&A*, **154**, 243
- Stahl, O., Jankovics, I., Kovács, J., et al. 2001, *A&A*, **375**, 54
- Sterken, C., Jones, A., Vos, B., et al. 1996, *IBVS*, **4401**, 1
- Thackeray, A. D. 1950, *MNRAS*, **110**, 524
- Tielens, A. G. G. M. 2005, *The Physics and Chemistry of the Interstellar Medium* (Cambridge University Press)
- Tielens, A. G. G. M., & Hollenbach, D. 1985, *ApJ*, **291**, 722
- Tody, D. 1986, in *Proc. SPIE Instrumentation in Astronomy VI*, ed. D. L. Crawford, **627**, 733
- Tody, D. 1993, in *Astronomical Data Analysis Software and Systems II*, eds. R. J. Hanisch, R. J. V. Brissenden, & J. Barnes, *ASP Conf. Ser.*, **52**, 173

- Tsamis, Y. G., Barlow, M. J., Liu, X.-W., Danziger, I. J., & Storey, P. J. 2003, [MNRAS](#), **345**, 186
- Ueta, T., & Meixner, M. 2003, [ApJ](#), **586**, 1338
- Umana, G., Buemi, C. S., Trigliolo, C., et al. 2009, [ApJ](#), **694**, 697
- Umana, G., Buemi, C. S., Trigliolo, C., et al. 2010, [ApJ](#), **718**, 1036
- Vamvatira-Nakou, C., Hutsemékers, D., Royer, P., et al. 2013, [A&A](#), **557**, A20
- van Genderen, A. M., The, P. S., Augusteijn, T., et al. 1988, [A&AS](#), **74**, 453
- van Genderen, A. M., Sterken, C., & de Groot, M. 1997, [A&A](#), **318**, 81
- Voors, R. H. M., Waters, L. B. F. M., de Koter, A., et al. 2000, [A&A](#), **356**, 501
- Weis, K. 2001, [Rev. Mod. Astron.](#) **14**, 261
- Weis, K. 2008, [ASPC](#), **388**, 231
- Weis, K. 2011, [IAUS](#), **272**, 372
- Wolf, B., & Stahl, O. 1982, [A&A](#), **112**, 111
- Wolf, B., Appenzeller, I., & Stahl, O. 1981, [A&A](#), **103**, 94
- Wood, H. E. 1914, [MNRAS](#), **74**, 698
- Yamamura, I., Makiuti, S., Ikeda, N., et al. 2010, AKARI/FIS All-Sky Survey Bright Source Catalogue, Version 1.0, Release Note
- Young Owl, R. C., Meixner, M. M., Fong, D., et al. 2002, [ApJ](#), **578**, 885

Appendix A: Tests of the dust model

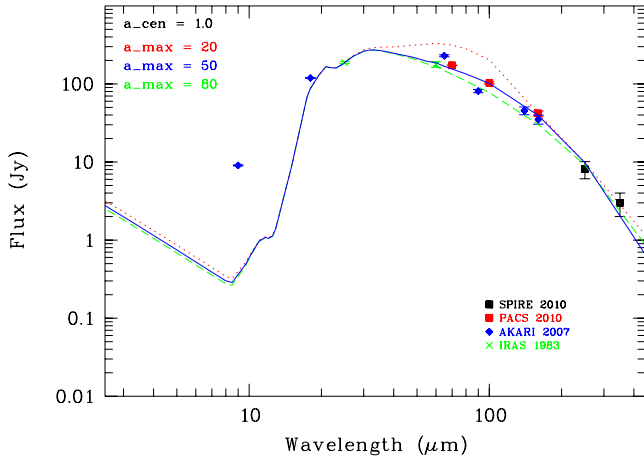


Fig. A.1. Fits of the far-infrared ($\lambda > 20 \mu\text{m}$) SED of the nebula around AG Car. The dust composition (optical constants of silicates with a 50/50 Mg-to-Fe abundance given by Dorschner et al. 1995) and a_{cen} are kept constant while the value of a_{max} changes.

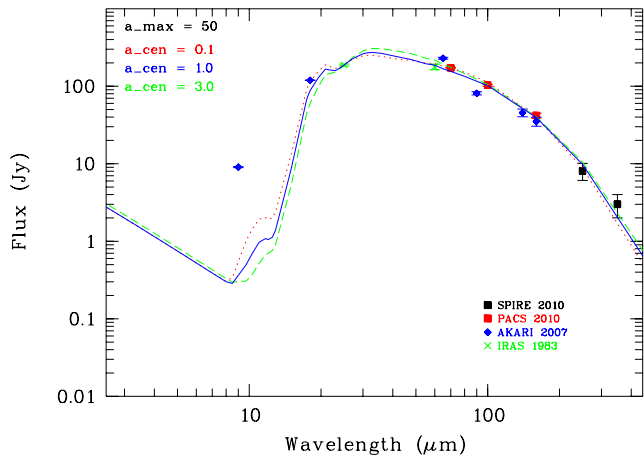


Fig. A.2. Fits of the far-infrared ($\lambda > 20 \mu\text{m}$) SED of the nebula around AG Car. The dust composition (optical constants of silicates with a 50/50 Mg-to-Fe abundance given by Dorschner et al. 1995) and a_{max} are kept constant while the value of a_{cen} changes.

In Sect. 4 the model of the dust nebula is presented and the necessity of a population of large dust grains is stressed. Several tests have been performed using the 2-Dust code in an effort to reproduce the observed data with different populations of dust grains from those adopted in Sect. 4. Our main concern was to investigate the influence of the dust grain size and composition on the model SED. For this reason, we calculated many models by changing one parameter and keeping the other ones constant. Keeping in mind that two different populations of grains were used to reproduce the broad observed SED in Sect. 4, we consider one population of small grains with radii $a_{\text{min}} < a < a_{\text{cen}}$ and one population of large grains with radii $a_{\text{cen}} < a < a_{\text{max}}$. For the dust composition, we used the optical constants given by Dorschner et al. (1995) for three different abundances of Mg to Fe, 0.5/0.5 (the model presented in Sect. 4), 0.4/0.6, and 0.8/0.2. For the dust grain sizes, the values of 20, 50, and 80 μm were considered for a_{max} and the values of 0.1, 0.3, 1, and 3 μm were considered for a_{cen} , with the value of a_{min} being kept constant and equal to 0.005 μm .

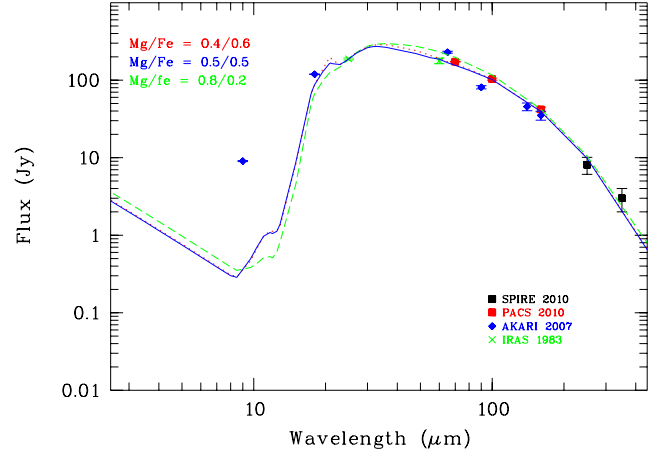


Fig. A.3. Fits of the far-infrared ($\lambda > 20 \mu\text{m}$) SED of the nebula around AG Car. $a_{\text{max}} = 50 \mu\text{m}$ and $a_{\text{cen}} = 1 \mu\text{m}$ are kept constant while the dust composition changes. The optical constants of silicates given by Dorschner et al. (1995) are used for different Mg-to-Fe abundances.

The comparison of these tests shows that large grains are necessary to reproduce the data. The influence of the change of a_{cen} on the fit of the observed SED is almost negligible. Furthermore, the fit depends little on the dust abundance of Mg to Fe. This is illustrated in Figs. A.1–A.3. In Fig. A.1 three dust models are illustrated. The dust composition is the same (optical constants of silicates with a 50/50 Mg-to-Fe abundance given by Dorschner et al. 1995) and the only parameter that changes is a_{max} . We see that better fits to the data are achieved when large grains are considered, in particular when $a_{\text{max}} = 50 \mu\text{m}$. In all cases, when adjusting the observed flux at 250 μm , a value for a_{max} that is too small ($< 20 \mu\text{m}$) gives too much flux at 60–100 μm . In Fig. A.2 the comparison of three models with the same a_{max} and dust composition but with different a_{cen} is illustrated. The model SED depends little on a_{cen} . In Fig. A.3 the comparison of three models with the same grain sizes but different dust composition (in terms of the abundance Mg to Fe) is illustrated. Again, the model SED depends little on this dust abundance ratio, with a slightly better adjustment for Mg/Fe = 50/50. We finally note that changing the power law index of the grain size distribution does not significantly affect these results.

Appendix B: Modified blackbody fit on the SED

The observed SED (Fig. 5) can also be reproduced with a simpler model that is the sum of two modified BB curves $F_{\nu} \propto B_{\nu}(T_{\text{d}})\nu^{\beta}$. Only the photometric points were considered for making the fit illustrated in Fig. B.1. The mass of the dust can then be derived using the equation

$$M_{\text{dust}} = \frac{F_{\nu} D^2}{B_{\nu}(T_{\text{d}}) \kappa_{\nu}}, \quad (\text{B.1})$$

where κ_{ν} is the mass absorption coefficient, i.e. the absorption cross section per unit mass, B_{ν} the Planck function and D the distance to the nebula (Hildebrand 1983). For this calculation, the two populations of dust grains are considered independently. The fluxes measured at 25 μm and 250 μm are used, i.e., at those wavelengths where the contribution of each population dominates (Fig. B.1). At 25 μm , $\kappa_{\nu} = 483 \text{ cm}^2 \text{ g}^{-1}$ for the silicates of Dorschner et al. (1995). For grains of radii smaller than the wavelengths at which dust radiates, κ_{ν} is roughly independent of the radius and behaves as ν^{β} in the far-infrared. However

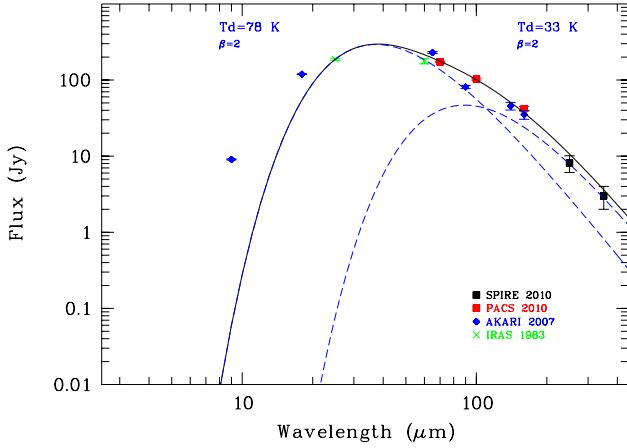


Fig. B.1. Same as Fig. 5 but the infrared SED of the nebula around the LBV AG Car is fitted by the sum of two modified blackbody curves.

the second population of dust grains involves large grains (up to $50 \mu\text{m}$) so that this hypothesis is no longer valid. The value of κ_ν is then taken from the 2-Dust results where it is explicitly

computed for the adopted grain population. At $250 \mu\text{m}$, $\kappa_\nu = 13.6 \text{ cm}^2 \text{ g}^{-1}$, which is significantly higher than expected under the small-grain approximation. With such large grains the frequency dependence of κ_ν also differs from the ν^2 law, being closer to ν^1 below $100 \mu\text{m}$. A fit with such a composite modified BB gives $T_{\text{dust},1} = 76 \text{ K}$ and $T_{\text{dust},2} = 31 \text{ K}$ (which is only slightly different from the values obtained with ν^2 only). Using $T_{\text{dust},1} = 76\text{--}78 \text{ K}$ and $T_{\text{dust},2} = 31\text{--}33 \text{ K}$ in Eq. (B.1), we then derive $M_{\text{dust},1} = 0.05\text{--}0.04 M_\odot$ and $M_{\text{dust},2} = 0.22\text{--}0.19 M_\odot$ for the small and the large grains respectively, in very good agreement with the 2-Dust results.

Appendix C: Emission line fluxes for each spaxel

The results of the emission line flux measurements for each spaxel are given in Table C.1. The first column contains the detected ions along with the spectral band in which the corresponding line was measured. The following columns contain the line fluxes, expressed in W/m^2 , along with their errors. The spaxel numbers (Fig. 6) are mentioned in every cell of the table. The quoted uncertainties are the sum of the line-fitting uncertainty plus the uncertainty due to the position of the continuum.

Table C.1. Line fluxes in each spaxel.

Ion	λ (band) (μm)	$F \pm \Delta F$ ($10^{-15} \text{ W m}^{-2}$)	$F \pm \Delta F$ ($10^{-15} \text{ W m}^{-2}$)	$F \pm \Delta F$ ($10^{-15} \text{ W m}^{-2}$)	$F \pm \Delta F$ ($10^{-15} \text{ W m}^{-2}$)	$F \pm \Delta F$ ($10^{-15} \text{ W m}^{-2}$)
		<u>spaxel 0,0</u>		<u>spaxel 0,1</u>	<u>spaxel 0,2</u>	<u>spaxel 0,3</u>
[O I]	63 (B2A)	–	0.40 ± 0.05	0.14 ± 0.05	–	–
[N II]	122 (R1B)	0.15 ± 0.02	1.15 ± 0.01	0.85 ± 0.02	0.56 ± 0.02	0.26 ± 0.02
[O I]	146 (R1B)	–	0.03 ± 0.01	–	–	–
[O I]	146 (R1A)	–	0.03 ± 0.01	–	–	–
[C II]	158 (R1A)	–	0.21 ± 0.01	0.13 ± 0.01	0.05 ± 0.01	–
[N II]	205 (R1A)	–	0.21 ± 0.05	0.11 ± 0.03	–	–
		<u>spaxel 1,0</u>		<u>spaxel 1,1</u>	<u>spaxel 1,2</u>	<u>spaxel 1,3</u>
[O I]	63 (B2A)	0.22 ± 0.05	0.65 ± 0.05	0.47 ± 0.05	0.29 ± 0.05	–
[N II]	122 (R1B)	0.64 ± 0.01	1.86 ± 0.02	1.49 ± 0.02	1.38 ± 0.01	0.61 ± 0.03
[O I]	146 (R1B)	0.02 ± 0.01	0.04 ± 0.01	0.04 ± 0.01	0.02 ± 0.01	–
[O I]	146 (R1A)	0.02 ± 0.01	0.04 ± 0.01	0.04 ± 0.01	0.03 ± 0.01	–
[C II]	158 (R1A)	0.09 ± 0.01	0.25 ± 0.01	0.24 ± 0.01	0.19 ± 0.01	0.06 ± 0.01
[N II]	205 (R1A)	0.10 ± 0.02	0.27 ± 0.07	0.29 ± 0.07	0.24 ± 0.06	0.14 ± 0.04
		<u>spaxel 2,0</u>		<u>spaxel 2,1</u>	<u>spaxel 2,2</u>	<u>spaxel 2,3</u>
[O I]	63 (B2A)	0.41 ± 0.05	0.26 ± 0.05	0.15 ± 0.05	0.65 ± 0.05	0.19 ± 0.05
[N II]	122 (R1B)	1.18 ± 0.02	1.43 ± 0.02	1.01 ± 0.02	1.63 ± 0.02	0.75 ± 0.01
[O I]	146 (R1B)	0.03 ± 0.01	0.02 ± 0.01	0.02 ± 0.01	0.04 ± 0.01	0.02 ± 0.01
[O I]	146 (R1A)	0.03 ± 0.01	0.02 ± 0.01	0.01 ± 0.01	0.05 ± 0.01	0.02 ± 0.01
[C II]	158 (R1A)	0.20 ± 0.01	0.24 ± 0.01	0.17 ± 0.01	0.30 ± 0.01	0.14 ± 0.01
[N II]	205 (R1A)	0.17 ± 0.04	0.35 ± 0.09	0.28 ± 0.07	0.33 ± 0.08	0.15 ± 0.04
		<u>spaxel 3,0</u>		<u>spaxel 3,1</u>	<u>spaxel 3,2</u>	<u>spaxel 3,3</u>
[O I]	63 (B2A)	0.25 ± 0.05	0.36 ± 0.05	0.60 ± 0.05	1.35 ± 0.06	–
[N II]	122 (R1B)	1.04 ± 0.02	1.56 ± 0.02	1.46 ± 0.02	1.68 ± 0.02	0.40 ± 0.01
[O I]	146 (R1B)	0.03 ± 0.01	0.02 ± 0.01	0.05 ± 0.01	0.07 ± 0.01	–
[O I]	146 (R1A)	0.02 ± 0.01	0.03 ± 0.01	0.04 ± 0.01	0.09 ± 0.01	0.02 ± 0.01
[C II]	158 (R1A)	0.16 ± 0.01	0.26 ± 0.01	0.32 ± 0.01	0.43 ± 0.01	0.13 ± 0.01
[N II]	205 (R1A)	0.16 ± 0.04	0.22 ± 0.06	0.23 ± 0.06	0.35 ± 0.09	–
		<u>spaxel 4,0</u>		<u>spaxel 4,1</u>	<u>spaxel 4,2</u>	<u>spaxel 4,3</u>
[O I]	63 (B2A)	–	–	0.58 ± 0.05	0.58 ± 0.06	–
[N II]	122 (R1B)	0.43 ± 0.02	0.66 ± 0.02	1.06 ± 0.02	0.49 ± 0.02	0.11 ± 0.02
[O I]	146 (R1B)	–	–	0.04 ± 0.01	0.03 ± 0.01	–
[O I]	146 (R1A)	–	–	0.04 ± 0.01	0.04 ± 0.01	–
[C II]	158 (R1A)	0.04 ± 0.01	0.09 ± 0.01	0.26 ± 0.01	0.22 ± 0.01	0.04 ± 0.01
[N II]	205 (R1A)	0.09 ± 0.02	–	0.17 ± 0.04	–	–

Notes. A dash indicates a poor signal-to-noise ratio or a nondetection. The spatial configuration corresponds to the footprint of the PACS-spectrometer as displayed in Fig. 6.